Thickness of Lunar Mare Basalts: New Results Based on Modeling the Degradation of Partially Buried Craters

Jun Du, Wenzhe Fa, Mark Wieczorek, Minggang Xie, Yuzhen Cai, Meng-hua Zhu

JGR Planets

RESEARCH ARTICLE
10.1029/2018JE005872

Key Points:
- Crater degradation theory and a new shape model of fresh craters are applied to estimate the thickness of lunar mare basalts
- The median thickness of sampled mare basalts is 105 m, roughly half as thick as those obtained when not considering crater degradation
- The eruption rate of mare basalts decreased with time, and the topographic diffusivity of lunar craters increases with crater diameter

Supporting Information:
- Supporting Information S1
- Table S1

Correspondence to:
J. Du,
jundu@pku.edu.cn

Citation:
Du, J., Fa, W., Wieczorek, M. A., Xie, M., Cai, Y., & Zhu, M.-H. (2019). Thickness of lunar mare basalts: New results based on modeling the degradation of partially buried craters. *Journal of Geophysical Research: Planets*, *124*, 2430–2459. https://doi.org/10.1029/2018JE005872

Received 8 NOV 2018
Accepted 19 AUG 2019
Accepted article online 27 AUG 2019
Published online 13 SEP 2019

Author Contributions
Funding Acquisition: Wenzhe Fa, Mark A. Wieczorek
Methodology: Jun Du, Wenzhe Fa, Mark A. Wieczorek, Minggang Xie, Meng-Hua Zhu
Validation: Jun Du, Wenzhe Fa, Mark A. Wieczorek, Minggang Xie, Yuzhen Cai
Supervision: Wenzhe Fa, Mark A. Wieczorek
Writing - review & editing: Jun Du, Wenzhe Fa, Mark A. Wieczorek

Thickness of Lunar Mare Basalts: New Results Based on Modeling the Degradation of Partially Buried Craters

Jun Du[1,2], Wenzhe Fa[1,3,4], Mark A. Wieczorek[2], Minggang Xie[3], Yuzhen Cai[1], and Meng-Hua Zhu[3,4]

[1]Institute of Remote Sensing and Geographical Information System, School of Earth and Space Sciences, Peking University, Beijing, China, [2]Université Côte d'Azur, Observatoire de la Côte d'Azur, CNRS, Laboratoire Lagrange, Nice, France, [3]State Key Laboratory of Lunar and Planetary Sciences, Macau University of Science and Technology, Macau, China, [4]CAS Center for Excellence in Comparative Planetology, Hefei, China

Abstract Partially buried craters on the Moon are those craters whose distal ejecta are covered by lava flows and where the crater rim crest still protrudes above the mare plain. Based on the difference in rim heights between a partially buried crater and an unburied crater, previous studies estimated the thicknesses of the lunar mare basalts. However, these studies did not consider the erosion of the crater rim height, which can result in an overestimate in the derived thickness. By using recent high-resolution topographic data, we report a basalt thickness estimation method based on numerically modeling the topographic degradation of partially buried craters. We identified 661 buried craters over the lunar surface, and their spatial distribution suggests a preferential occurrence along the mare-highland boundaries. An elevation model of fresh lunar craters was derived, and the topographic diffusion equation was used to model crater degradation. By modeling the formation, degradation, and flooding of partially buried craters, basalt thicknesses were estimated for 41 mare craters whose rims are completely exposed. The resulting mare basalt thicknesses vary from 33 to 455 m, with a median value of 105 m that is 95 m smaller than that derived when not considering crater degradation. The estimated eruption rate of lunar mare basalts is found to have peaked at 3.4 Ga and then decreased with time, indicating a progressive cooling of the lunar interior. As a by-product from the crater degradation model, our results suggest that the topographic diffusivity of lunar craters increases with diameter.

Plain Language Summary The thickness of mare basalts that partially cover a lunar crater can be estimated from the crater shape. To simplify this problem, previous studies used the shape of a fresh lunar crater, which had been well-characterized beforehand. In reality, however, the lunar crater degrades with time, which results in a more complicated, time-dependent crater shape. In this study, a crater degradation model is used to better estimate mare basalt thicknesses. Our results show that the mare basalt thickness could be overestimated by a factor of two when crater degradation is not considered. Our results constrain the volcanic eruption rate with time and imply that the crater degradation rate scales with crater size.

1. Introduction

Impact cratering and volcanism are the two major processes shaping the surface of the Moon. Impact cratering created large topographic relief on the lunar surface, whereas volcanic products filled in the topographic lows and produced new surfaces. Impact cratering and volcanism also act on each other as well. On the one hand, impact cratering produced stress conditions in the crust that favor the ascent of the magma (Michaut & Pinel, 2018). On the other hand, lavas might either partially or completely bury a previously formed impact crater depending on the thickness of the flow and the height of the crater rim. As a result, the observed lunar surface morphology and size-frequency distribution of lunar craters have been evolving due to the combined effect of crater formation and mare emplacement.

The lunar maria are composed of iron-rich basalts that were originally generated by partially melting the mantle, then driven by excess pressure at or below the crust-mantle boundary to propagate upward through dikes, and finally extruded out to form larger-scale, effusive plains over the lunar surface (e.g., Head, 1976; Head & Wilson, 2017; Wilson & Head, 1981, 2017). Radiometric measurements of lunar samples and crater

counting of basaltic units suggest that most of the mare basalts erupted from 4 to 1.2 Ga (e.g., Head, 1976; Hiesinger et al., 2011) with a few exceptions of extremely old and young basaltic units being recorded. For example, rare basaltic clasts in lunar meteorites have ages as old as 4.36 Gyr (Snape et al., 2018), some pre-basin basalts referred to as cryptomaria are known to be covered by ejecta from basins such as Imbrium and Orientale (Bell & Hawke, 1984), and some isolated irregular mare patches were dated to be around 50 Myr in age (Braden et al., 2014). The volume of lunar mare basalts is of great scientific significance, because it can constrain the thermal evolution of the Moon, reveal the sources and styles of volcanism, and contribute to the subsequent tectonic activity and lithospheric deformation (Head, 1982; Solomon & Head, 1979, 1980). As a first-order approximation, the volume of mare basalts can be simply estimated as the product of their surface area and thickness. In early studies, the total surface area of mare basalts was estimated to be about 6.2×10^6 km^2, covering ~17% of the lunar surface (Head, 1975). The mare basalt thickness, however, varies from place to place, from several meters to several kilometers.

In this study, we focus on using the morphology of impact craters that are partially buried by lava flows, in order to estimate the thickness of lavas that were emplaced after the crater formed. On the Moon, the continuous ejecta blanket of a normal, unflooded crater usually extends about one crater radius from the crater rim (Moore et al., 1974). A partially buried crater forms when a lava flow covers the distal low-elevation ejecta, leaving the high-elevation rim crest visible (e.g., Baldwin, 1970; Eggleton, 1961; Marshall, 1963). Note that craters could also be infilled or buried by ejecta from nearby craters (Xie & Zhu, 2016), but craters partially buried by ejecta deposits will not be considered in this study. The mare basalt thickness surrounding a partially buried crater can be calculated if two quantities are known: the total rim height as defined by the elevation difference between the rim crest and preflooding background surface, and the exposed rim height with respect to the present-day surroundings (De Hon, 1974). The resulting thickness estimate can be either the total basalt thickness if the partially buried crater formed initially on the highlands, or the thickness of the upper basaltic layers if the partially buried crater formed on the maria. In practice, the exposed rim height was easily measurable, whereas the total rim height was estimated based on the observed morphology of fresh craters. Previous studies used scaling relations between crater rim height and diameter of fresh lunar craters (e.g., Baldwin, 1949, 1963; Pike, 1967, 1972, 1977) to estimate the total rim height and hence the basalt thickness. Using early topography data (e.g., Lunar Topographic Orthophotomap/LTO and Lunar Astronautical Chart/LAC), mare basalts near partially buried craters in the western (45°S–45°N; 90°W–10°E) and eastern (30°S–30°N; 0–100°E) maria were estimated to be 400 and 200 to 400 m thick on average, respectively (De Hon, 1979; De Hon & Waskom, 1976).

However, craters on the Moon suffer from continual meteoroid bombardment and other mass-wasting processes. As a result, with increasing time, the crater diameter should increase and the rim height should decrease due to the downslope movement of rim and ejecta materials. If the initial rim height were used to determine the basalt thickness, then the basalt thickness would be overestimated if the crater erosion were significant. To account for crater degradation, Hörz (1978) randomly selected 82 highland craters with different degradation states and measured their rim heights. As the obtained median rim height is only 58% of that for fresh lunar craters (Pike, 1977), Hörz (1978) then simply reduced all the basalt thickness estimates in De Hon and Waskom (1976) and De Hon (1979) by a factor of two. The resulting, revised median mare basalt thickness on the lunar nearside was found to be smaller than 300 m. Nevertheless, the classification of ages and degradation states for the lunar highland craters in Hörz (1978) was largely qualitative.

Based on the morphologic characteristics of the inner wall, rim crest, and ejecta deposits, several criteria were proposed to categorize lunar craters into different degradation states in a qualitative way (e.g., Baldwin, 1949; Basilevsky, 1976; Pohn & Offield, 1970). Crater degradation is mainly caused by diffusive and nondiffusive processes. Micrometeoroid bombardment, thermal expansion and contraction, and seismic shaking have been modeled as diffusive processes, whereas landslides that occur when the surface slope reaches a critical value and emplacement of ejecta from adjacent craters are considered as nondiffusive processes (Melosh, 2011; Fassett & Thomson, 2014). Modeling efforts have typically used the classical diffusion equation (e.g., Craddock & Howard, 2000; Culling, 1960, 1963; Richardson, 2009; Soderblom, 1970), and the most recent efforts have made use of high-quality topography data sets of the Moon (e.g., Fassett & Thomson, 2014; Xie & Zhu, 2016).

In this study, we developed an improved method for mare basalt thickness estimation based on the elevation profile of partially buried impact craters. By applying topographic diffusion theory, the evolution of a partially buried crater can be modeled through time, both before and after the emplacement of the mare basalts. The modeled final elevation profile depends on the initial crater topographic profile, the basalt thickness, the time durations between crater formation, flooding and the present, and the topographic diffusivity. By comparing the observed profile with a series of modeled profiles, the mare basalt thickness can be estimated at the location of the partially buried crater. Our study improves upon previous works in several ways. First, the previous databases of partially buried craters were constructed several decades ago (e.g., De Hon, 1979; De Hon & Waskom, 1976), and new remote sensing data with unprecedented spatial resolution and quality have since been acquired. Second, crater degradation modeling has been improved through the years (e.g., Fassett & Thomson, 2014), and high precision digital elevation models allow us to better characterize the morphology of both fresh and degraded impact craters. Third, depending on whether the partially buried crater formed on highland or mare materials (as determined from remote sensing data), this technique may provide not only the thickness of the uppermost basaltic units that embayed the crater but also the total thickness of basalts that erupted in the region. Fourth, based on the best fitting parameters from the degradation model, we are able to investigate how the topographic diffusivity varies with both time and crater size.

The structure of this paper is organized as follows. First, we summarize prior methods that have been used to estimate the thicknesses of the mare basalts on the Moon (section 2). Second, we present all the remote sensing data sets and the derived data products that will be employed in this study, including their resolution, coverage, and precision (section 3). Third, the identification criteria and a detailed classification of buried craters are presented, and the statistical characteristics of the buried crater population are analyzed (section 4). Next, the mare basalt thickness estimation method is described, including the topographic diffusion model, the initial profile of fresh craters, and the numerical inversion scheme (section 5). After that, the estimated mare basalt thicknesses are presented and analyzed, which includes a detailed case study and the global results (section 6). Then, the obtained mare basalt thicknesses are compared with those derived using other techniques, the cumulative basalt volume and time-dependent eruption rate of the mare basalts are calculated, and as a by-product, the scale dependence of the crater degradation process is discussed (section 7). Finally, we conclude by discussing several remaining issues, as well as the outlooks for other applications of the crater degradation model (section 8).

2. Methods to Estimate Mare Basalt Thicknesses

Mare basalt thicknesses have been investigated by many studies, which can be divided into four general classes: direct measurements using elevation differences of lava flow fronts and layering features in crater walls (e.g., Robinson et al., 2012; Schaber, 1973; Stickle et al., 2016), subsurface sounding radar using a spaceborne or ground penetrating radar (e.g., Oshigami et al., 2014; Phillips et al., 1973; Xiao et al., 2015), geophysical techniques based on seismology and gravity (e.g., Cooper et al., 1974; Gong et al., 2016; Talwani et al., 1973), and investigations of impact craters, including partially buried craters, modification of the crater size-frequency distribution, and the composition of crater ejecta (e.g., De Hon, 1974; Hiesinger et al., 2002; Thomson et al., 2009). Each of these methods measures a different "thickness" (total thickness, thickness of the last flow, or thickness since a crater formed), and has different spatial and temporal resolutions. As a result, the global volume of mare basalts is still poorly constrained.

The most straightforward technique for estimating basalt thicknesses is the direct measurement of the height of a lava flow front and layering structures in lava tube skylights and crater inner walls. This method usually gives the thicknesses of younger lava flows close to the lunar surface. Using the shadow length measurement technique with Apollo 14–17 metric photographs and Lunar Orbiter (LO) images, the individual lava flows in Mare Imbrium were estimated to be 1–96 m in thickness (Gifford & El-Baz, 1981; Schaber, 1973). Three lava tube skylights have been spotted in Marius Hills, Mare Tranquillitatis, and Mare Ingenii using the Lunar Reconnaissance Orbiter Camera/Narrow Angle Camera (LROC/NAC) images. Their steep inner walls consist of five to eight layers that were found to be 3–14 m in thickness based on shadow length measurements (Robinson et al., 2012). Layering structures were also found in the crater walls of 13 fresh lunar craters. The flow thicknesses at these impact sites were estimated to be 48–400 m based on the LROC/Wide Angle Camera (WAC) digital terrain model (DTM) and LROC/NAC images (Stickle et al., 2016). However,

it should be noted that few optical images are favorable for the recognition of such layering structures and shadow length measurements (Hiesinger et al., 2011).

Thanks to the penetration capability of radar waves, subsurface reflectors can be directly observed by spaceborne radar sounders and ground penetrating radars. The basalt thickness can be determined by converting the apparent depth of subsurface reflections to the actual depth using an assumed dielectric permittivity. The observed thickness of mare basalts could be the total thickness or only the thickness of superficial layers depending on the penetration depth of the radar wave. Based on the 5-MHz Apollo 17 Lunar Sounder Experiment data and assuming a dielectric permittivity of 8.7, subsurface reflectors were identified at mean depths of 0.9 and 1.6 km in southern Mare Serenitatis (Peeples et al., 1978; Sharpton & Head, 1982), at a mean depth of 1.4 km in Mare Crisium (Peeples et al., 1978), and at depths of 0.6–1.0 m in Oceanus Procellarum (Cooper et al., 1994). In the 5-MHz Selenological and Engineering Explorer/Lunar Radar Sounder (SELENE/LRS) data, one to five basaltic layers were detected with thicknesses of 73–460 m in several nearside maria (Ishiyama et al., 2013; Kobayashi et al., 2012; Ono et al., 2009; Oshigami et al., 2009, 2012, 2014). The Chang'E-3 Lunar Penetrating Radar also performed subsurface sounding experiments along its survey track (near 44.12°N, 19.51°W), and the 60-MHz observations revealed multiple layering structures in the mare basalts. Zhang et al. (2015) found three basalt layers with thicknesses of 25, 130, and 195 m, and Xiao et al. (2015) identified four basalt layers with thicknesses of 42, 80, 100, and 120 m. We note that the estimated mare basalt thickness from radar observations depends on the poorly constrained dielectric permittivity (Ishiyama et al., 2013) and that signal artifacts produced by the radar itself make it difficult to detect deep-seated reflectors (Li et al., 2018).

Geophysical techniques based on gravity and seismology data have also been used to investigate basalt thicknesses. These methods depend on the density contrast between mare and highland materials, and therefore can provide the total basalt thickness. Using the seismic refraction data collected at the Apollo 17 landing site, the total basalt thickness near the Taurus-Littrow valley was estimated to be 1.4 km (Cooper et al., 1974). With newly acquired gravity data from the Gravity Recovery and Interior Laboratory (GRAIL) mission, the total basalt thickness on the western nearside hemisphere (19°S–45°N, 68°W–8°W) was estimated to be 740 m on average (Gong et al., 2016). Though the seismic estimate is applicable for a small region near the Apollo 17 landing site, the gravity inversions provide average thicknesses over circular regions with radii between 240 and 600 km (Gong et al., 2016). It should be noted that results based on geophysical techniques sometimes depend on poorly constrained properties such as the density and porosity of the subsurface materials.

Impact craters excavate materials from depths of about one tenth of their diameter and thus provide a window on the composition of materials below the surface (Croft, 1980; Melosh, 1989). For craters in the maria, the presence (or not) of anorthositic highland materials in the ejecta blanket constrains the total thickness of mare basalts at the impact site. For example, based on the FeO abundances derived from the Clementine Ultraviolet/Visible (UVVIS) images, the total basalt thicknesses in parts of Mare Imbrium and Mare Humorum were estimated to be respectively 1.5–2 km and 150–500 m (Budney & Lucey, 1998; Thomson et al., 2009). Mare basaltic flooding can also affect the size-frequency distribution of craters found on a geologic unit. During the emplacement of lava flows, some portion of the smallest craters are completely buried. The existence of such a discontinuity in the crater size-frequency distribution can be used to estimate the flow thickness (Neukum & Horn, 1976). This method returns the thickness of the uppermost, youngest lava flows. For several nearside mare regions, modifications of the crater size-frequency distributions have been identified, and the basalt thicknesses therein were estimated to be 20 to 220 m (Hiesinger et al., 2002). We need to stress that the basalt thickness estimated from impact craters also invokes a better, quantitative understanding of the crater ejecta emplacement and topographic degradation mechanisms.

3. Data Sets

Multiple remote sensing data sets are used in this study, and generally they can be categorized into four classes: optical images, topographic data, surface composition, and radar sounding observations. The first three types of data are used to identify partially buried craters over the lunar surface. The topographic data are used to extract the radial profiles of fresh craters and partially buried craters for initial crater profile modeling and basalt thickness estimation, respectively. The compositional data are used to determine the target

materials (mare/highland) over which a partially buried crater formed, and to derive the dielectric permittivity for the estimation of the actual depth of subsurface reflectors in radar images. The radar sounding data are used to compare with the mare basalt thickness estimates from partially buried craters.

The final global LROC/WAC mosaics with a spatial resolution of 100 m/pixel are used in our study, which have been photometrically corrected with favorable solar incidence angles of 55—75° for morphology recognition (Robinson et al., 2010; Speyerer et al., 2011). Previous studies suggested that at least 10 pixels are needed to identify a small lunar crater unambiguously (e.g., Fa et al., 2014; Fassett, 2016; Robbins et al., 2014), and therefore, we restrict our analysis to craters larger than 1 km in diameter.

Recent, widely used lunar topographic data sets include the LRO/Lunar Orbiter Laser Altimeter (LOLA) digital elevation model (DEM; Smith et al., 2010) and the SELENE/Terrain Camera (TC) stereo-image-derived digital terrain model (Haruyama et al., 2012). With a vertical accuracy of 1 m and covering the entire lunar surface, the LOLA DEM has a geodetically accurate global control network, and the gridded data products were produced with a nominal spatial resolution of 29.6 m at the lunar equator (Smith et al., 2010). The SELENE/TC DTM has a vertical accuracy of 10 m, covers the nonpolar region (<60°N/S), and has a higher spatial resolution of 10 m (Haruyama et al., 2012). To combine the advantages of these two data sets, a SELENE-LRO merged digital elevation model (SLDEM) was generated by coregistering the TC DTM to the LOLA geodetic framework (Barker et al., 2016). The resulting data set covers latitudes between 60°N/S with a spatial resolution of 59 m and a vertical accuracy of 3–4 m (Barker et al., 2016). In this study, the SLDEM was used as the elevation data for latitudes equatorward of 60°, and the LOLA DEM with a spatial resolution of 60 m was used for higher latitudes.

The elevation data used by De Hon in his series of studies come from three sources (De Hon, 1979). As the first choice, he used the Lunar Topographic Orthophotomap to calculate rim heights where the Apollo 15–17 mapping photographs were available. This data product consists of contours with an interval of 100 m and has an elevation uncertainty of 30–115 m (Defense Mapping Agency Topographic Center, 1973). In regions beyond those pictured by the Apollo mapping cameras, the author used the Lunar Astronautical Chart derived from Earth-based telescopic photography or measured the shadow lengths in the Lunar Orbiter frames to extract rim heights. The Lunar Astronautical Chart has a sparser contour interval of 300 m (Aeronautical Chart Information Center, 1973), and both derived elevations have an uncertainty of 100 m (De Hon, 1979). It should be noted that the above elevation uncertainties of the LTO, LAC, and LO data are nominal values and that the resulting, measured morphometric parameters could have an average uncertainty as large as 700 m in regions with significant relief (see Table 1 in Pike, 1974). In comparison with these early topographic data sets used by De Hon, the newly acquired SLDEM and LOLA data have much better spatial resolution (2–5 times higher), coverage (globally covered), and accuracy (8–40 times higher). Therefore, the basalt thickness estimates given by our study should be considered to supercede those obtained by De Hon's pioneering studies (e.g., De Hon, 1979; De Hon & Waskom, 1976).

Using multispectral data collected by the SELENE/Multiband Imager (MI; Ohtake et al., 2008) and the Clementine/UVVIS (Eliason et al., 1999), FeO and TiO_2 abundance maps can be calculated. The uncertainties of the FeO abundance are 0.8 wt.% for the MI and 1.0 wt.% for the UVVIS data sets, whereas the uncertainties for TiO_2 are, respectively, 0.4 wt.% and 0.9 wt.% (Lucey et al., 2000; Otake et al., 2012). The recently released MI mineral abundance mosaics cover the lunar surface between 50°N/S with a spatial resolution as high as 60 m/pixel and include photometric corrections using surface topography (Lemelin et al., 2016). The UVVIS composition maps have a lower spatial resolution of 200 m/pixel and are not topographically corrected, but they have better coverage at latitudes higher than 50° in comparison to the MI maps (Eliason et al., 1999). Therefore, in this study we will use the MI abundance maps for regions equatorward of 50° latitude and the UVVIS composition maps at higher latitudes.

The SELENE LRS operated at a center frequency of 5 MHz with a bandwidth of 2 MHz, resulting in a 75-m range resolution in vacuum. After surface clutter reduction with synthetic aperture radar (SAR) processing techniques, the final released data have an along-track resolution of 600 m (Kobayashi et al., 2012). The LRS data provide the received backscattered echo as a function of time delay. The data formats include the one-dimensional A-scope plot (where the radar echo strength at a given location is plotted against time delay), and the two-dimensional SAR-processed image (where the radar echo strength is plotted with the along-track distance and the time delay). To convert apparent depth, which is the product of half the time

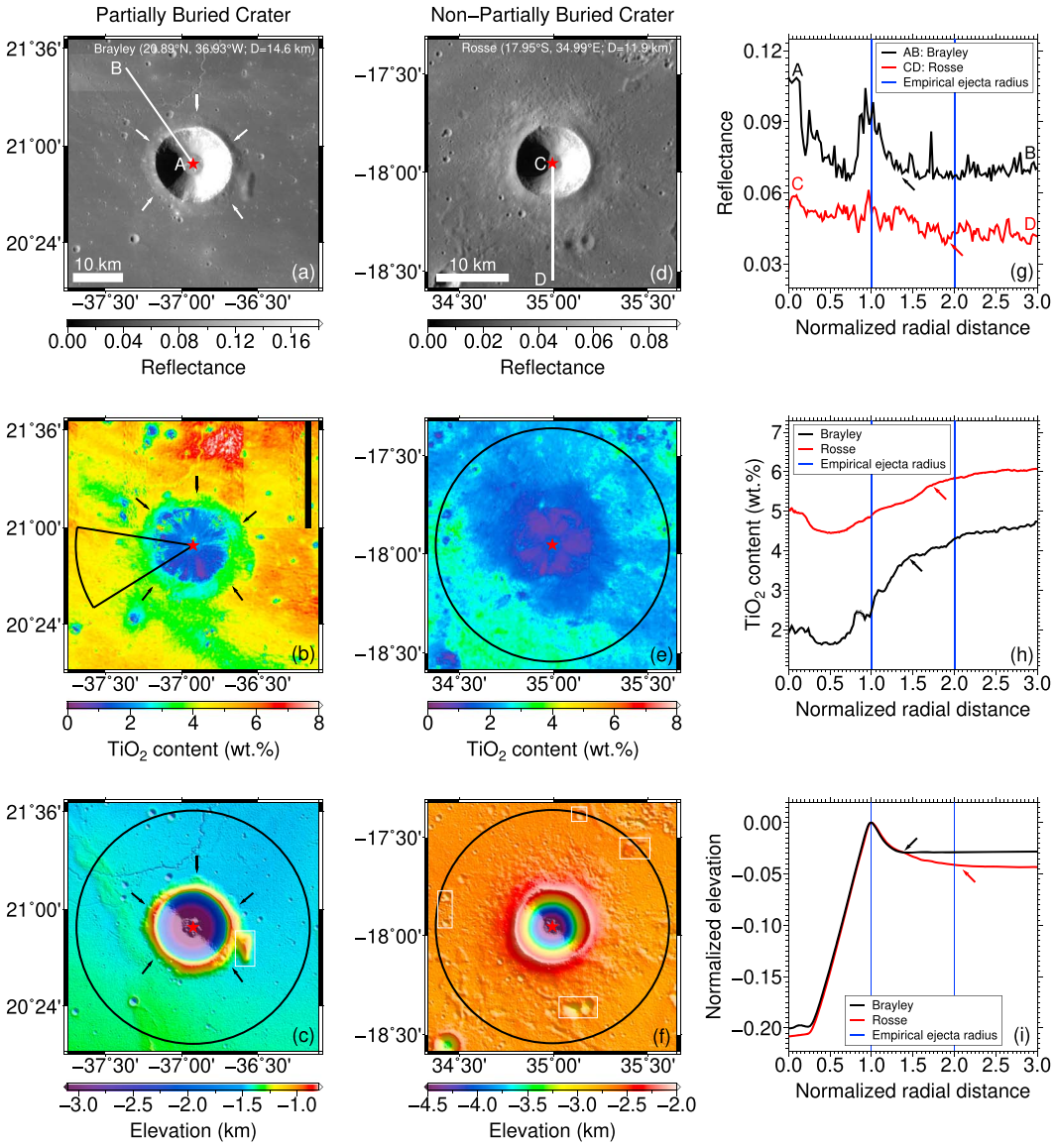

Figure 1. Example of a partially buried crater Brayley (D = 14.6 km) and a normal, unburied crater Rosse (D = 11.9 km). LROC/WAC reflectance, SELENE/MI-derived TiO_2 content, and SLDEM elevation maps for Brayley (a–c) and Rosse (d–f) are shown in the top, middle, and bottom rows, respectively. The right column plots selected individual radial profiles (AB and CD) of reflectance (g), and the azimuthally averaged radial profiles of TiO_2 content (h) and elevation (i), for Brayley (solid black lines) and Rosse (solid red lines). In (a–f), the red stars denote the location of crater centers. In (b), (c), (e), and (f), the solid black lines give the boundaries where the azimuthally averaged radial profiles were extracted. In (a–c), the white and black arrows indicate the boundaries of the crater ejecta. In (c) and (f), the white boxes are areas excluded when calculating elevation profiles. In (g–i), the black and red arrows point to the manually identified ejecta boundaries for Brayley and Rosse, respectively, and the solid blue lines denote the crater radius and the predicted continuous ejecta radius for unburied crater ejecta. All the y axes in the profile plots refer to the case of Brayley, and for Rosse, the reflectance and TiO_2 content profiles have been shifted arbitrarily for clarity. All the profiles are plotted with the radial distance normalized by crater radius, and the elevation profile is plotted with the vertical elevation normalized by crater diameter. The rim crest elevation of Brayley was set to be 0, and the crater profile of Rosse was shifted vertically to have the same rim crest elevation as Brayley.

delay and the speed of light in vacuum, to actual depth, the vertical profile of dielectric permittivity (often assumed to be constant) for the studied region is required.

Two derived data products are also used in this study to aid our understanding of the geological context of partially buried craters. A mare basemap derived from the monochromatic and color ratio images from the LROC/WAC and Clementine/UVVIS data sets provides the locations of regions flooded by mare basalts (Nelson et al., 2014). The boundaries of individual basaltic units defined by the LROC/WAC and Clementine/UVVIS data products are also used to determine the surface unit that embayed the partially buried crater (Hiesinger et al., 2006, 2011; Morota et al., 2009, 2011; Pasckert et al., 2018). The absolute model age of each unit was derived from the crater-counting results (Hiesinger et al., 2006, 2011; Morota et al., 2009, 2011; Pasckert et al., 2018).

4. Craters Buried by Mare Basalts

4.1. Identification of Buried Craters

Partially buried craters are impact craters that have been partially covered by lava flows, and whose crater rim is at least partially protruding above the surrounding lavas (De Hon, 1974). By this definition, two criteria are proposed for the identification of a partially buried crater: (1) the transition between crater ejecta and postimpact lava flows should be abrupt and well defined, and (2) the extent of the exposed proximal ejecta should be smaller than one crater radius. The first criterion is a result of the fact that ejecta deposits grade smoothly from continuous to discontinuous deposits. Lava flows that embay the crater simply truncate the preexisting ejecta. The second criterion is a result of the fact that continuous ejecta of unburied lunar craters usually extend about one crater radius from the crater rim (Moore et al., 1974).

Evidences for these two diagnostic characteristics can be found easily in the reflectance, composition, and elevation maps of impact craters. As an example, in Figure 1, the partially buried crater Brayley (20.89°N, 36.93°W; $D = 14.6$ km) and the unburied crater Rosse (17.95°S, 34.99°E; $D = 11.9$ km) are selected here for a detailed comparison. Both craters are simple craters with a bowl shape and a similar size. The ejecta boundary of Brayley is seen to have an abrupt boundary in the reflectance, TiO_2 content, and elevation data (arrows in Figures 1a–1c). In contrast, the crater ejecta of Rosse gradually degrade to the background terrain, and the ejecta boundary is not well defined (Figures 1d–1f). The ejecta radii of Brayley (black) and Rosse (red) were obtained by using the abrupt changes in the reflectance, TiO_2 content, and elevation radial profiles (Figures 1g–1i). For the crater Brayley, the radial profiles reach the background level at about 1.4 times the crater radius (black arrows), whereas for the crater Rosse, the ejecta boundaries (red arrows) are difficult to determine but are with no doubt larger than those of Brayley.

Because the crater diameters of Brayley and Rosse are similar, a comparison of the exposed rim heights derived from the elevation profiles can provide additional evidence on the burial of Brayley's ejecta by lava flows. In this study, the azimuthally averaged radial profile of the crater is used to calculate its rim height, which is defined as the elevation difference between the rim crest and the background terrain as averaged within 2.5–3 crater radii from the crater center. The exposed rim height of Brayley is estimated to be 415 m, in comparison with 512 m for Rosse. Since Brayley is about 2.7 km larger and also appears morphologically younger (shaper rim crest and more prominent streaks of fresh boulders in the crater inner wall) than Rosse, the most likely explanation for the smaller exposed rim height of Brayley is the emplacement of lava flows exterior to the crater rim.

4.2. Database and Classification of Buried Craters

We constructed a database of buried impact craters (Figure 2), making use of the LROC/WAC basemap and the ArcGIS platform with the Crater Helper Tools toolkit (Nava, 2011). In order to obtain the center and diameter of the crater, the crater rim needs to be determined first. The crater rim can be seen as an exposed crater rim (Figure 1a), a wrinkle ridge (Figure S1e) or a topographic depression boundary (Figure S1f). If the crater rim is intact and continuous, then three control points that are ~120° apart along the rim were selected manually to define a circle that was used to determine the center and diameter of the crater. When less than 10% of the crater rim can be seen, then the determination of the crater center and diameter is problematic: we did not include this type of crater in our study, which may result in an underestimate of the total number of partially buried craters. In total, we identified 661 partially and completely buried craters on the lunar surface, all located within mare deposits or along mare margins. The diameter, longitude,

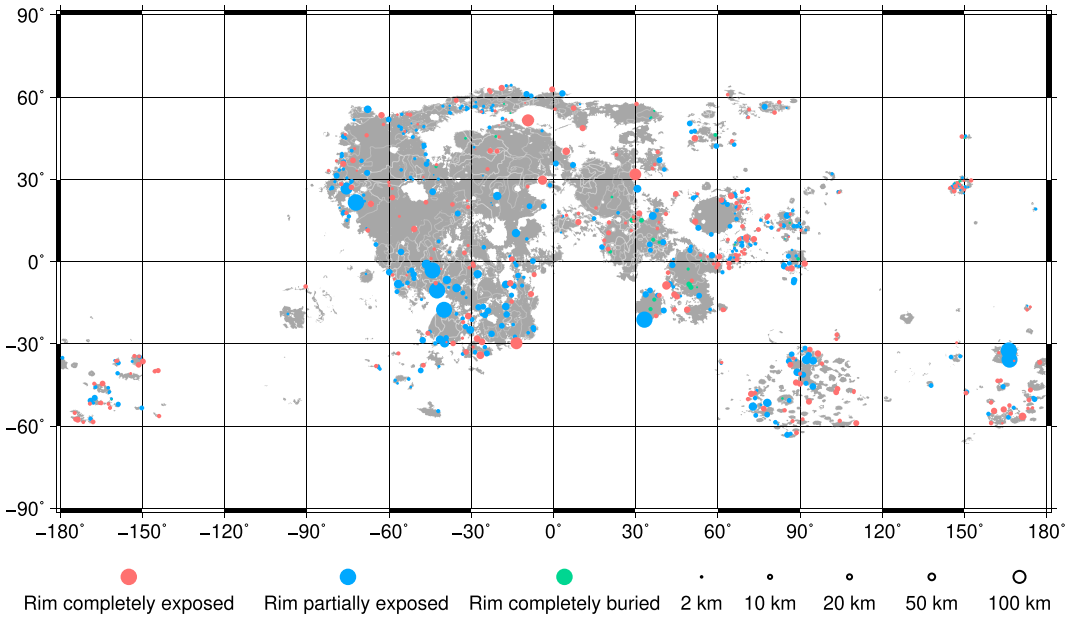

Figure 2. Distribution of buried craters with completely exposed rims (light red, $N = 262$), partially exposed rims (blue, $N = 360$), and completely buried rims (green, $N = 39$). The lunar maria basemap (gray) is from Nelson et al. (2014), and the basaltic unit boundaries (white) are from a compilation of previous studies (Hiesinger et al., 2006, 2011; Morota et al., 2009, 2011; Pasckert et al., 2018). The size of the circles increases with increasing crater diameter.

latitude, classification, percentage of the rim that is buried, and composition of the rim/ejecta are given in the supporting information.

We divided the identified buried craters into three classes based on the observed morphology of the crater rim: completely exposed, partially exposed, and completely buried (Table 1). Craters with rims completely or partially exposed can be classified into two subclasses based on their locations. If the entire exposed ejecta are surrounded by lava flows, then the crater is classified as being located in the mare, whereas if part of the exposed ejecta are contiguous with the surrounding highland terrain, then the crater is classified as being located on the mare-highland boundary. We note that craters located in the maria could have formed on the highland crust and later were flooded by basalts, such that the exposed crater rim and ejecta have a highland composition (see section 5.4).

In an idealized case, a crater would form on a perfectly flat surface, the rim crest height would be the same everywhere, and any mare basalts that flooded the region would be uniform in thickness. There are several factors that complicate such an idealized scenario. First, the impact crater could form on a sloping surface and the lavas would only embay that portion of the crater at the lowest elevations. This is likely what occurred for partially buried craters that form along the mare-highland boundaries. In these cases (Figure S1a), the

Table 1
Classification of Buried Impact Craters ($N = 661$)

Class	Location	Description	Number
Rim completely exposed	Mare (Figure 1a)	Rim and proximal ejecta completely exposed, distal ejecta buried	74
	Mare-highland boundary (Figure S1a)	Mare side: rim and proximal ejecta completely exposed, distal ejecta buried; Highland side: rim and ejecta completely exposed	188
Rim partially exposed	Mare (Figure S1b)	Rim and proximal ejecta partially exposed, distal ejecta buried	112
	Mare-highland boundary	Mare side: rim and proximal ejecta partially exposed ($N = 239$; Figure S1c) or completely buried ($N = 9$; Figure S1d), distal ejecta buried; Highland side: rim and ejecta completely exposed	248
Rim completely buried	Mare	Rim and ejecta completely buried, characterized by a wrinkle ridge (Figure S1e) or an interior topographic depression (Figure S1f)	39

crater rim and ejecta can be divided into highland and mare parts: the crater ejecta of the highland part are not buried by lava flows, whereas the crater ejecta of the mare part are. Though these craters are included in our database, they will not be analyzed later as a result of this complication.

In a more complex scenario, a part of the crater rim could be breached by the exterior lavas in several places, leaving a crater rim that is discontinuous (Figures S1b–S1d). The formation of such a partially buried crater could arise as a result of several asymmetric processes. The crater rim height is not everywhere constant, either as a result of the initial formation processes or by later erosional processes (such as small craters that formed on the rim). Alternatively, the basalt thickness might not be uniform everywhere, with the thicknesses being higher on the side of the crater rim that was breached.

To extend our database, we also searched for craters that are completely buried by lava flows. This type of crater is usually characterized by a concentric wrinkle ridge over the crater rim (Figure S1e) or a subtle topographic low in the crater interior as a result of thermal contraction of the cooling lava flow (Figure S1f). The mare basalt thickness around a completely buried crater is difficult to estimate. On the one hand, the mare basalt thickness needs to be greater than the crater rim height. On the other hand, this crater rim height could have been degraded between the times of crater formation and lava infill. Therefore, although we include these entirely buried craters in our database, we will not use them later when estimating mare basalt thicknesses. We note that completely buried craters can also sometimes be identified in the Bouguer gravity anomaly maps (e.g., Evans et al., 2016, 2018; Sood et al., 2017; Zhang et al., 2018).

De Hon and Waskom (1976) and De Hon (1979) constructed a global partially buried crater database that included 342 partially buried craters in the nearside eastern (30°S–30°N; 0–100°E) and western (45°S–45°N; 90°W–10°E) maria, of which the crater rim is either completely or partially exposed as defined by our classification. It is challenging to directly compare their database with ours, because there is a misregistration between the two databases in the coordinate systems used. By comparing the provided crater center coordinates for several of the largest and thus least ambiguous partially buried craters (e.g., Flamsteed P: $D = 108.9$ km), this misregistration can be up to 10 km. Nevertheless, our database is expected to be more accurate and more complete than previous ones, because of our use of more recent remote sensing data sets with considerably higher accuracy and resolution.

4.3. Spatial Distribution and Statistics of Buried Craters

The most prominent feature seen in the spatial distribution of buried craters is their preferential occurrence along the mare-highland boundaries (Figure 2). This distribution pattern is to be expected, since the mare basalts at the edge of the mare are expected to be thinner than elsewhere. Though the thicker flows in the mare centers can entirely flood craters of a given size, the thinner flows at the margins can only partially flood the crater. This interpretation is supported by the identification of ghost craters in Bouguer gravity anomaly maps in the central portions of the maria (e.g., Evans et al., 2016, 2018; Sood et al., 2017; Zhang et al., 2018). We also note that the smallest buried craters are distributed uniformly across the mare, whereas larger ones are concentrated along the mare-highland boundaries. Our interpretation of this observation is that the larger craters were completely buried in the central mare where the basalt thicknesses are the greatest. Many of the smaller craters, in contrast, are younger and formed during the main phase of mare volcanism. Many of these craters thus formed on top of preexisting lava flows. The thickness of the flows that buried these craters was thus only a fraction of the total thickness of lavas in the region. With thinner flows embaying the crater, the probability that the rim crest would remain unburied would be higher.

Histograms of the different classes of buried craters as a function of diameter are shown in Figure 3a. The diameters of all the partially and completely buried craters range from 1.5 to 130 km, of which craters with rims completely exposed in the maria range from 1.8 to 45.3 km. In general, the peak in the histogram is skewed toward smaller craters. This is in part because there are in general more smaller than larger craters, but also because the older and larger craters that formed before the main phase of mare volcanism have been completely buried. Analyzing the craters by class, the median crater diameter is found to increase from craters with rims completely buried (3.7 km), to those with rims partially exposed (9.3 km), and to those with rims completely exposed (11.6 km). This observation is easy to explain: for a given thickness of lava flow, smaller craters with lower rim heights are easier to completely bury than larger craters with greater rim heights. In terms of location, the median diameter of partially and completely buried craters on maria (6.6 km) is smaller than that along mare-highland boundaries (12.9 km). As noted previously, we interpret

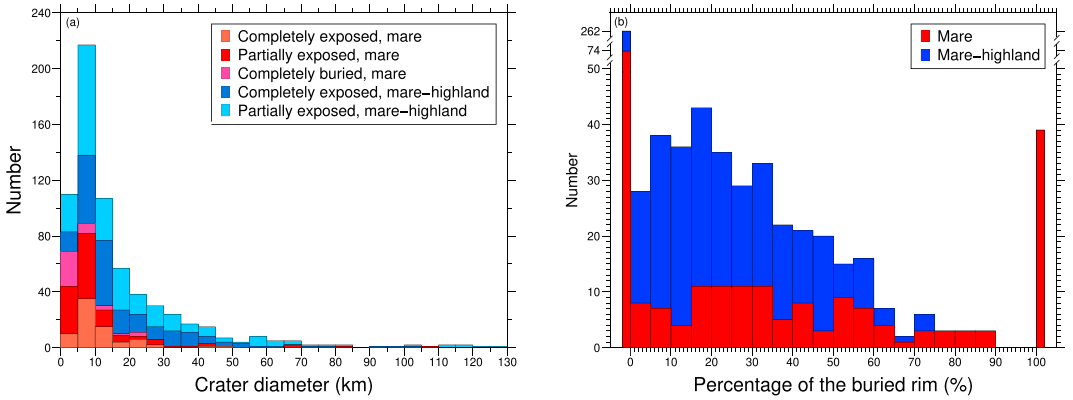

Figure 3. (a) Size-frequency distributions of the different classes of buried craters. (b) Percentage of the rim buried by mare basalts for craters that formed in the mare (red) and craters that formed along the mare-highland boundary (blue). In (b), the scale of the vertical axis is discontinuous, and the total numbers of craters with rims completely exposed or completely buried are plotted in the leftmost and rightmost bins, respectively.

this observation as being a result of the mare basalts being thicker in the center of the mare than those along their edges, therefore older, larger craters inside the maria are completely buried.

For all of the partially buried craters in our database, we have estimated the percentage of the crater rim crest circumference that was buried by lava flows (Figure 3b). The median percentage of rim burial of mare craters (24%) is larger than that of mare-highland boundary craters (7%). This is simply because the crater rim is never buried on the highland side of the mare-highland boundary. This figure also shows that we did not include any craters where more than 90% and less than 100% of the rim has been buried. Although we did find some short exposed crater rims that might indicate the presence of partially buried craters with rim exposure smaller than 10%, we are not confident to determine the crater center and diameter because no other indicators of the crater rim (e.g., wrinkle ridges or a topographic depression) were found that can help to outline the crater.

5. Mare Basalt Thickness Estimation

5.1. Method Overview

We develop a method for determining the thickness of mare basalts that partially bury a crater. This method uses an initial crater topographic profile, and crater degradation is accounted for by use of a diffusive topographic degradation model. Topographic degradation occurs both before and after the emplacement of the mare basalts. Model parameters include the initial diameter of the crater (D_{init}), the time at which the crater formed (t_{c}), the time when the mare basalts were emplaced (t_{b}), the thicknesses of the basalts exterior and interior to the crater rim (T_{ext} and T_{int}), and diffusion parameters that determine the rate of the topographic degradation between crater formation and lava emplacement (κ_{c}) and after lava emplacement (κ_{b}). Model parameters are then determined by minimizing the root-mean-square difference (σ) between the modeled final topographic profile (H_{final}) and the observed profile (H_{obs}):

$$\sigma = \sqrt{\sum_{i=1}^{N} \left[H_{\mathrm{final}}\left(D_{\mathrm{init}}, T_{\mathrm{ext}}, T_{\mathrm{int}}, \kappa_{\mathrm{c}} t_{\mathrm{c}}, \kappa_{\mathrm{b}} t_{\mathrm{b}}, z_0; i\right) - H_{\mathrm{obs}}(i)\right]^2 / N} \quad (1)$$

where z_0 is a vertical offset between the modeled final and the observed profiles, and i is the ith of N points along the profile. Calculation of H_{final} and extraction of H_{obs} are discussed in section 5.4. Though we can also solve for the thickness of mare basalts that erupted interior to a crater's rim, this will not be discussed further.

Before estimating the basalt thickness exterior to the crater rim, we first calculate the FeO content of the crater rim. This step determines the composition of the surface on which the crater formed (i.e., mare or highland), which is necessary because the initial crater profile for fresh craters is slightly different in the highlands and maria (see Text S2.3 in the supporting information). Next, we mask out atypical features such as nearby craters, wrinkle ridges, and sinuous rilles. After this is done, we then produce the azimuthally averaged radial topographic profiles for the observed partially buried craters.

Given an initial crater profile (see section 5.2), we next make use of a topographic degradation model to determine how the profile varies with time. Micrometeoroid bombardment is thought to be one of the major processes that degrade craters. It can be modeled as a diffusive process, where ejecta that are newly excavated by small craters trigger downslope movement under the influence of gravity. Other processes, such as seismic shaking, can also be modeled as a diffusive process. We thus make use of the standard diffusion equation to model the evolution of surface topography (Culling, 1960):

$$\frac{\partial H}{\partial t} = \kappa \nabla^2 H \tag{2}$$

where H is the elevation of the studied crater, t is time, and κ is the effective diffusivity of all combined degradation mechanisms. We note that this approach neglects nondiffusive processes, such as burial by thick impact ejecta deposits, the formation of large craters on top of the crater being modeled, and landslides (see Richardson, 2009). Regardless, given that we mask out most regions affected by these processes when constructing the radial topographic profile, the neglect of nondiffusive processes should not affect our results in any significant manner. The above equation can be solved analytically in a cylindrical coordinate system, and the solution can be expressed as the sum of a series of Bessel functions (Xie & Zhu, 2016).

To obtain the final modeled profile, we need two steps of crater degradation. Before the eruption of the mare basalts, the initial condition is the topographic profile of the newly formed, fresh crater. After the basalt emplacement, the initial condition is the topographic profile of the crater that was just flooded by mare basalts, and then the present-day profile can be solved. Once the observed profile and a series of modeled profiles are acquired, the basalt thickness can be estimated by finding those parameters that minimize the difference between the modeled and observed profiles.

5.2. Shape of Fresh Craters

Before solving the topographic diffusion equation, we require an initial condition for the topographic profile of a fresh impact crater. Previous studies of crater degradation investigated simple mare craters ($0.8 \leq D \leq 5$ km; Fassett & Thomson, 2014) and complex highland craters ($20 \leq D \leq 166$ km; Xie & Zhu, 2016), whereas our partially buried craters cover a diameter range of 1.5 to 130 km and formed on both mare and highland crust. Therefore, we need to develop a more complete series of initial crater topographic profiles for fresh impact craters. Since the crater morphology depends on crater diameter and target properties (Melosh, 1989), six types of initial crater profiles were produced in this study, including simple ($1 \leq D \leq 15$ km), transitional ($15 < D \leq 20$ km), and complex ($D > 20$ km) craters, each over the maria and highlands. For consistency with our crater degradation model, all crater profiles will be based on azimuthal averages of the observed topography.

In optical images of the Moon, rays emanating from young craters for several crater radii can be seen that result from fresh crater ejecta and secondary craters. Craters with optical rays are considered to be young (<1 Gyr; Werner & Medvedev, 2010) and these optical rays fade with time due to micrometeoroid bombardment and space weathering processes (Hawke et al., 2004). In a recent global search for rayed craters (Werner & Medvedev, 2010), 1,211 craters larger than 1 km in diameter were identified, from which we extracted their topographic profiles. First, craters that formed on tilted background terrain, crater/basin rim, and wrinkle ridges were removed from the database. Then, atypical features around each crater were further excluded to eliminate large-scale topography variations on the background.

In total, 57 optical rayed craters were finally selected (Figure S2), with crater diameters ranging from 1.7 to 96 km for mare craters, and from 1.4 to 139 km for highland craters. For simple craters, the morphologies are known to be diameter independent, and we rescaled the height by the crater diameter and the radial distance by the crater radius (Fassett & Thomson, 2014). As in Fassett and Thomson (2014), cubic functions were used to fit the observed profiles. For transitional and complex craters, we first derived the diameter dependence of six morphometric parameters (central peak height, central peak radius, crater floor radius, crater depth, rim height, and continuous ejecta radius). Using these key parameters, the topography of the crater was modeled as a piece-wise function using exponential functions. The detailed procedures are given in the supporting information (Text S2), and the initial crater profiles (Figure 4) can be obtained using the formulas and coefficients in Tables A1 and A2.

When estimating the basalt thickness exterior to the crater rim, the variation of the crater rim height with crater diameter and degradation state is our primary concern. Our parameterization of crater shape shows

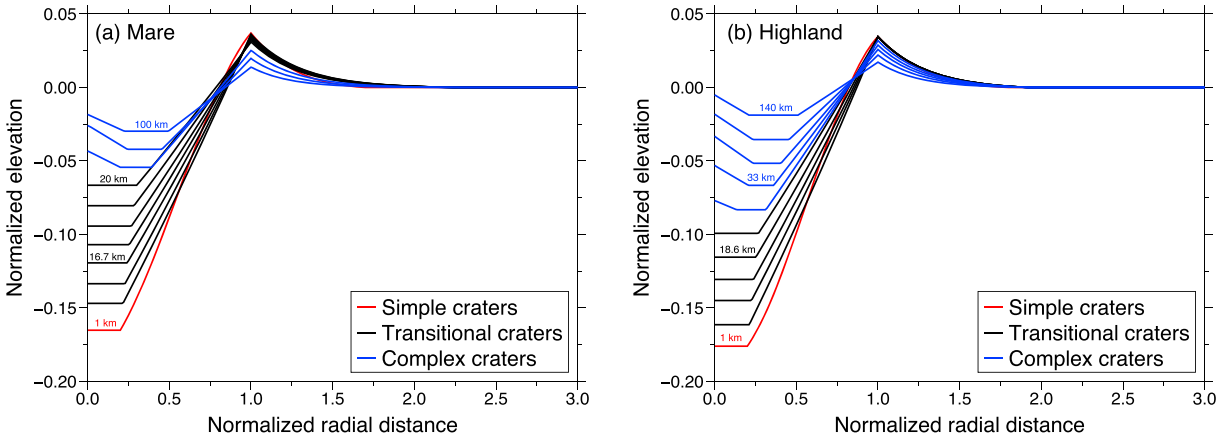

Figure 4. Radial elevation profiles for fresh lunar craters that formed on the mare (a) and highland (b). The radial distance is normalized by crater radius, and the elevation is normalized by crater diameter. The red curves denote simple craters, the black curves are transitional craters, and the blue curves represent complex craters. The plotted initial crater diameters were carefully selected to present the results for clarity and are labeled for several curves.

that the rim height increases from 37 m to 1.4 km and from 35 m to 1.9 km for mare and highland craters with diameters of 1–100 km, respectively. For simple fresh craters, the rim height of mare craters is always slightly larger than that of highland craters (37 m vs. 35 m at 1 km, and 555 m vs. 518 m at 15 km). For transitional and complex fresh craters, the rim height of mare craters decreases with respect to highland craters with increasing diameter, becoming smaller than highland craters at 17 km (Figures S3a and S4a).

As a comparison with a previous study, we note that our rim heights and those of Fassett and Thomson (2014) differ by less than 3 m for simple mare craters. When compared with the rim heights for complex highland craters in Xie and Zhu (2016) where the rim height-crater diameter relation was taken from Pike (1977), the difference first varies from 0 to 178 m with diameters of 1 to 33 km, and then increases from 0 to 705 m with diameters of 33 to 139 km. The discrepancy with the later study might arise from the following factors. First, the geologic context of highland craters is more complicated than that of mare craters, and different studies might apply different strategies to determine the background elevation and hence the rim height. Second, the topography data used and the fresh craters selected are also different. We selected 22 highland craters in the SLDEM and LOLA data and made use of azimuthally averaged profiles to calculate the rim height, which is defined as the elevation difference between rim crest and background surface (averaged from 2.5 to 3 crater radii). Pike (1977) chose 38 mare and highland craters in the Lunar Topographic Orthophotomap to derive the rim height, which is defined as the mean elevation at the crater rim minus that at the exterior rim flank foot. A more detailed comparison of crater topographic profiles between the two studies is found in Text S2.5 of the supporting information.

Regardless of any differences with previous studies, our derived morphometric parameters of fresh impact craters and the resulting initial crater profiles represent a distinct improvement. Our results are the first to consider not only the size dependence of crater morphology (simple, transitional, and complex) but also the target type (mare and highland). Our results are based on the freshest impact craters and should be more accurate than many previous investigations as we used newly acquired, high-quality elevation data sets and excluded surrounding atypical features. Lastly, we imposed the fitting functions at the simple-transitional, and transitional-complex boundaries to be continuous so that there are no abrupt changes in morphometric parameters at 15- and 20-km diameters.

It should be noted that even though we selected fresh craters with simple geologic contexts to investigate the initial crater rim height/diameter relation, natural variability of this quantity should be expected for any given crater diameter. Such variability could be the result of different impact conditions (including impact velocity and impact angle), as well as different target properties (such as porosity). This variability is quantified in Table A3, where we provide the root-mean-square deviation of the measured initial rim height with respect to the predicted initial rim height as a function of crater diameter. We note that the natural variability is similar for both mare and highland craters, so we combine them into one larger data set for analysis. In particular, for simple, transitional, and complex (smaller than 50 km in diameter) craters, the natural variabilities of the initial rim height are less than 73, 125, and 271 m, respectively.

5.3. Effect of Crater Degradation on Rim Height

Given an initial crater profile, we model the crater degradation process and estimate the reduction in the rim height. As a consequence of crater degradation, the rim crest moves both downward and outward (Figure S9). In an elevation profile, this process can be seen as the rim crest at an initial position (D_0, h_0) moving to ($D_0 + \Delta D$, $h_0 - \Delta h$), where D_0 and h_0 are initial crater diameter and rim height, and ΔD and Δh are the increase in crater diameter and the decrease in rim height due to the erosion process. Previous studies (e.g., De Hon & Waskom, 1976; De Hon, 1979), however, used the current crater diameter ($D_0 + \Delta D$) to estimate the initial rim height. Since the current rim diameter will always be larger than the initial rim diameter, this approach will overestimate the initial height of the crater rim.

We note that the manner by which the rim height degrades with time will be discontinuous at the simple-transitional transition at 15 km. In particular, as shown in Figures S3 and S4, the rim height to crater diameter ratio is constant for all simple craters, but this ratio decreases for craters with larger diameters. In addition to this, the formulas of the crater topographic profiles interior and exterior to the crater rim also change across this morphologic transition, as we used two different connecting functions for the crater inner wall and ejecta in the simple and transitional crater regimes (Table A1). The resulting discontinuous change in slopes to each side of the rim has a strong effect on how simple and transitional/complex craters degrade. It is for this reason that we will demonstrate the degradation of simple and larger craters separately.

The effect of topographic degradation on the crater rim height (Δh) is shown in Figure 5. In the upper two panels, we plot the reduction in rim height as a function of time over the past 3.9 billion years using a diffusivity of 5.5 m^2/Myr (Fassett & Thomson, 2014). Results for representative crater diameters of 5, 10, 15, 20, 50, and 100 km are plotted, and we emphasize that these diameters correspond to the initial diameter (and not the final eroded diameter). For simple craters, the reduction in rim height is nearly independent of diameter. After 3.9 billion years of erosion, the rim height reduction is about 45 m for a mare crater, and 41 m for a highland crater. For transitional and complex craters, the amount of rim erosion is largest for the smallest craters, and smallest for the largest craters. Small craters simply erode faster than large craters, in part because the surface slopes decrease with increasing diameter. For mare craters, the rim erosion is about 40 m for a 20-km-diameter crater and 31 m for a 50-km-diameter crater. For highland craters, these values are larger by about 20 % and 16%.

In the lowermost panel of Figure 5, we demonstrate how the rim erosion depends upon the assumed diffusivity. For this plot, we considered values of 5, 10, 25, 50, and 100 m^2/Myr, and then plotted the rim erosion associated with a simple 10-km-diameter mare crater. The result shows that if this crater formed at 3.9 Ga, then the reduction in rim height could range from 43 to 184 m with an increasing diffusivity. We note that the erosion of a crater depends only upon the product of the diffusivity and time and that these two parameters are hence not independent.

Previous basalt thickness estimates that did not consider crater degradation lie between 200 and 400 m (De Hon & Waskom, 1976; De Hon, 1979). For a diffusivity of 5.5 m^2/Myr, our results show that the rim height could be reduced by up to 45 m for a 3.9-Gyr-old, 10-km-diameter mare crater (Figure 5a). However, the amount of rim erosion increases substantially with increasing diffusivity. For a diffusivity of 100 m^2/Myr, Figure 5c shows that the rim height reduction could be 184 m, which is comparable to the basalt thicknesses that were previously estimated by De Hon and Waskom (1976) and De Hon (1979).

5.4. Estimation of Mare Basalt Thicknesses

The first step in estimating the initial topographic profile of a partially buried crater is to determine whether the crater formed on a mare or highland target. The composition of the rim and proximal ejecta of the identified crater is used to determine the composition of the target. The FeO content of mare materials is typically greater than 18 wt.%, whereas that of the highland crust is typically less than about 10 wt.% (Heiken et al., 1991). We use the intermediate value of 14 wt.% to discriminate between the two target compositions.

Next, we need to extract the azimuthally averaged radial elevation profiles of the partially buried craters. The elevation data were first extracted within a circular region that extends three crater radii from the crater center. Then, we excluded atypical topographic features such as small young impact craters, rilles, and faults. Finally, we defined a maximum radial range for each profile by looking for any abrupt changes in slope that might result from either a nonflat initial surface or postimpact modification processes. Only the elevations with radial distances smaller than this maximum range are compared with the modeled profiles when estimating the basalt thickness. Among the 74 mare craters with rims completely exposed to be studied, 11 of

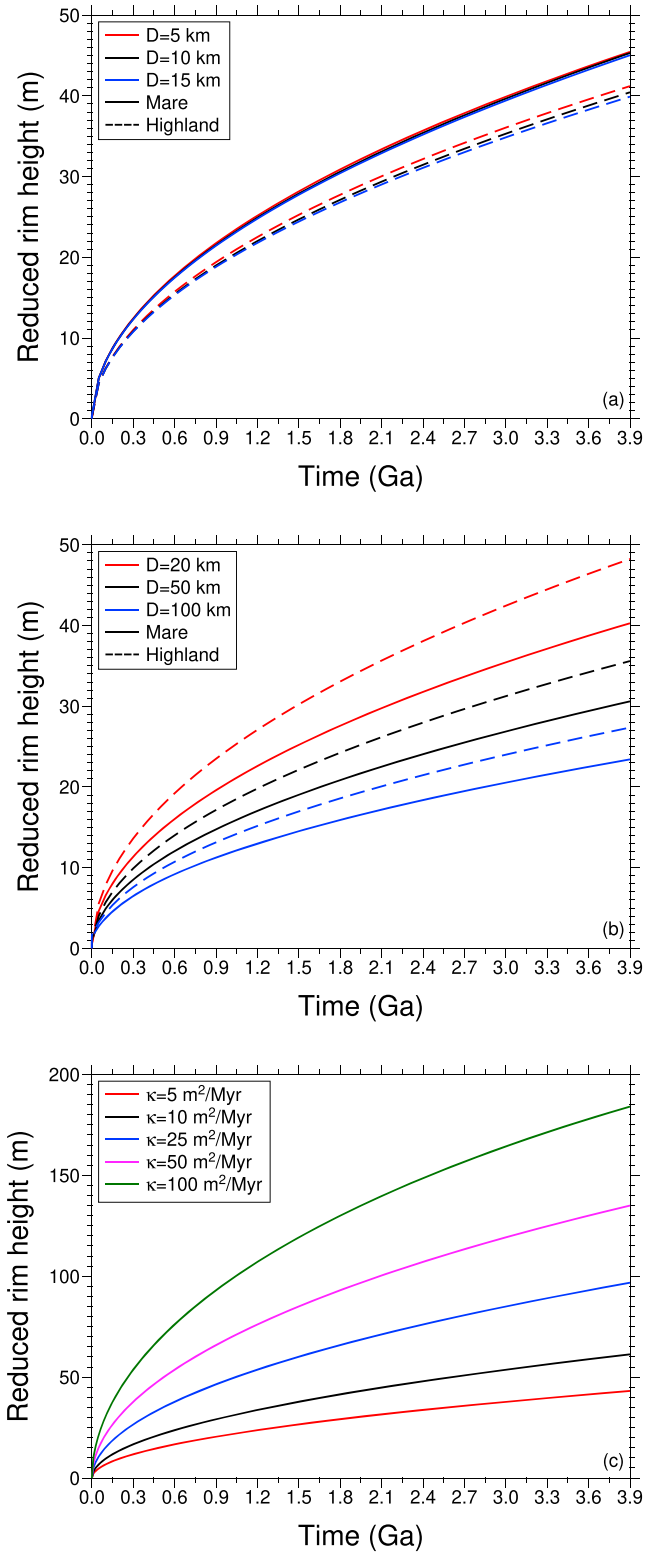

Figure 5. Predicted absolute rim height reduction during the degradation process. In (a) and (b), the diffusivity was set to 5.5 m^2/Myr and the results are plotted for several mare and highland craters with different diameters in simple (a) and transitional/complex regimes (b). In (c), results are plotted for a 10-km-diameter mare crater for several different diffusivities.

them have maximum radial ranges smaller than two crater radii. In this study, the radial profiles of craters smaller than 18 km in diameter were binned with a width of 100 m, whereas for craters larger than 18 km in diameter, the radial profiles were binned within 300 equally spaced annuli.

In our simulations, we used the products of diffusivity and time between crater formation and basalt emplacement $K_c = \kappa_c t_c$ and after basalt emplacement $K_b = \kappa_b t_b$ as model parameters. This is because the product of the two completely determines the topographic degradation, and we have few constraints on either the ages or diffusivities. For simplicity, and with no impact on our determination of the thickness of the basalts exterior to the crater, we assume that any basalts interior to the crater rim were emplaced at the same time as those exterior to the rim.

Our estimation method quantifies the misfit between the observed and modeled profiles as a function of six model parameters (see equation (1)). The initial crater diameter (D_{init}) must be smaller than the final diameter (D_f), and we investigated a range from $0.6D_f$ to D_f with a step size of 0.1 km. The exterior basalt thickness (T_{ext}) must be less than the initial rim height (h_r), so we investigated values from 0 to h_r with a step size of 1 m. The interior basalt thickness needs to be less than the depth of the crater floor below the rim crest (d_{cf}), and we investigated values up until this value with an interval of 1 m. The topographic profile of a partially buried crater was initially shifted to a vertical position where the background (2.5 to 3 crater radii) elevation is 0, and later the vertical offset parameter z_0 was allowed to vary from the lowest elevation (h_r–d_{cf}) to the highest elevation (h_r) along the profile with a step size of 1 m. The upper limit of the product of diffusivity and time after crater formation ($K_{max} = K_c + K_b$) is more difficult to constrain a priori. Nevertheless, it was suggested that the diffusivity could be expressed as the product of the diffusivity at a reference scale (e.g., 1 km) and the crater diameter to the power of about 1 (Xie et al., 2017). In our simulations, K_{max} for crater formation was assumed to be equal to $5.5 \times 3{,}900 \times D_f$ m^2, where 5.5 m^2/Myr is a reference diffusivity for a 1-km crater (Fassett & Thomson, 2014) and 3,900 Myr is an upper limit for the crater age in our study (Stöffler & Ryder, 2001). We used a step size of 500 m^2 for the diffusivity-time product. After performing our simulations, we checked to ensure that our chosen maximum value for the product did not correspond to the best fitting value and that the maximum value was sufficient to obtain an error bar for the diffusivity-time product.

Two of the outputs from the basalt thickness estimation model are the products of diffusivity and time before ($K_c = \kappa_c t_c$) and after ($K_b = \kappa_b t_b$) the emplacement of mare basalts. If an age for the mare basalts can be obtained, such as from crater counting, then it would be possible to determine the absolute value of the topographic diffusivity. In particular, the average diffusivity since the eruption of the basalts is given by $\kappa_b = K_b/t_b$. Furthermore, if we assume that the diffusivity was constant at all time ($\kappa_c = \kappa_b$), then we can estimate when the crater formed ($t_c = (K_c + K_b)/\kappa_b$).

When performing the numerical inversion for the best fitting parameters and uncertainties, one would ideally like to perform a global exhaustive search of the parameter space. Given the number of free parameters and their extensive ranges, however, this task would have been computationally prohibitive. In order to reduce the computation time, a global optimization algorithm using the sequence quadratic polynomial technique (Schittkowski, 1986) was used to search for the best fitting model parameters in the six-dimensional parameter space. This method uses a series of quadratic polynomial functions to approximate the nonlinear objective function, and the global optimal solution is found by searching along the direction with the largest gradient in the model parameter space. In this study, the Global Optimization Toolbox in MATLAB (MathWorks Inc, 2017) was used to solve this optimization problem.

We tested the applicability of this optimization algorithm in two different ways. First, we conducted a forward simulation of a 3-Gyr-old, 10-km-diameter mare crater that was embayed by basalt flow with an assumed thickness of 43 m, and then ran the global optimization toolbox to search for the basalt thickness. The result shows that the obtained basalt thickness differs only by 1 m with respect to the true value. Second, we varied the number of starting points used to initialize the optimization in the toolbox where each starting point consists of initial guesses for the six parameters in equation (1). We increased the number of starting points from 20 to 100 and set the initial values to be uniformly distributed in the parameter space. We found that, although different starting points gave slightly different results, the final results were all within the uncertainties obtained from our numerical inversion, as described below. Therefore, we can conclude that this global optimization toolbox converges adequately to the global minimum.

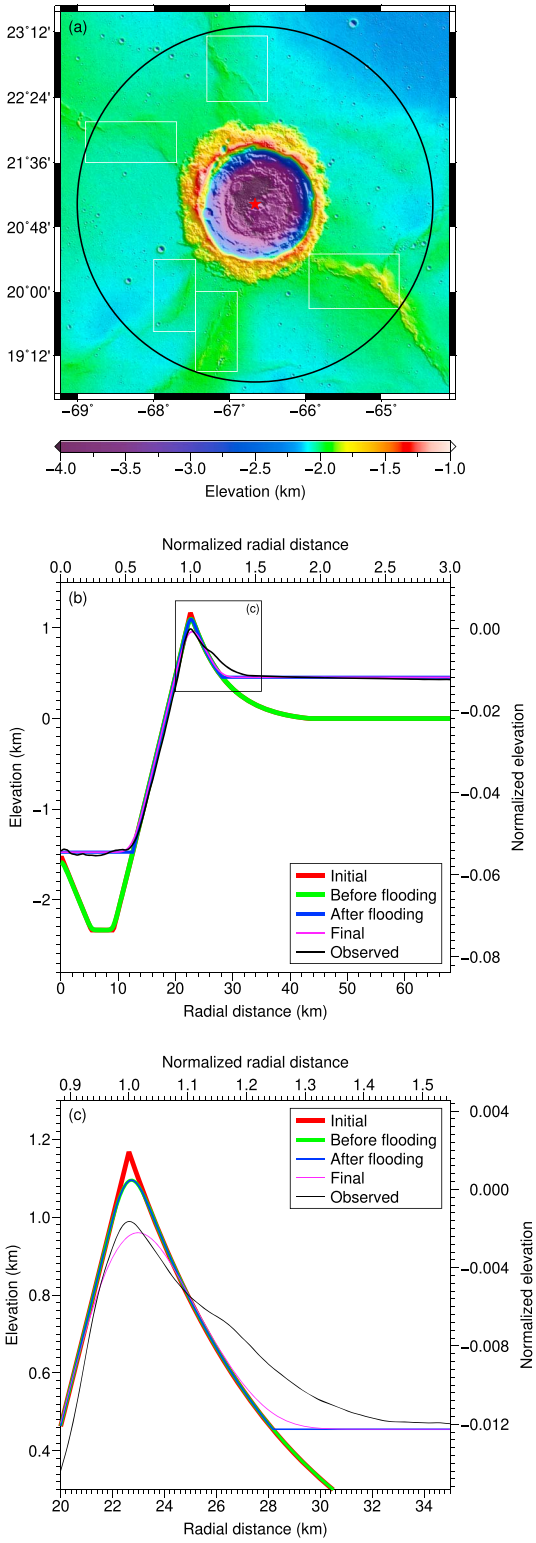

Figure 6. Elevation map (a) and radial elevation profiles at different points in time (b and c) for the crater Seleucus (D = 45.3 km). In (a), the red star denotes the crater center, the black solid circle shows the boundary within which the azimuthally averaged radial profile was extracted, and the white boxes show the regions excluded from the elevation data. In (b) and (c), the red, green, blue, magenta, and black curves represent the initial crater profile, the profile just before mare flooding, the profile just after mare flooding, the final present-day profile, and the observed profile. Panel (c) shows a zoom-in around the crater rim, which corresponds to the black box in (b).

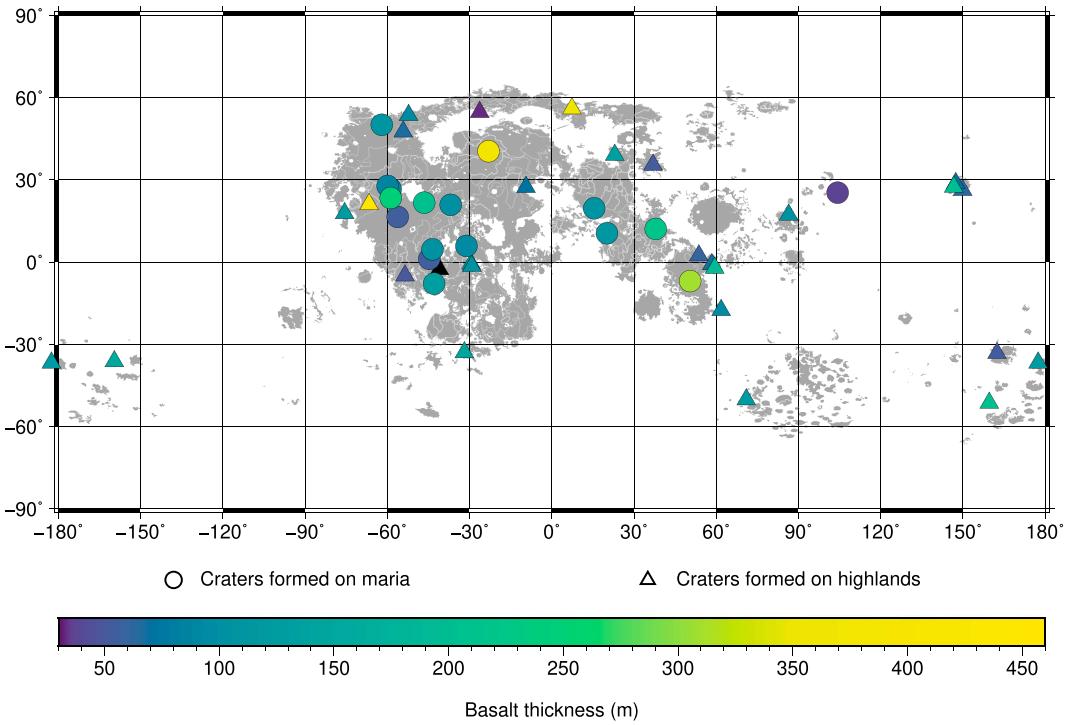

Figure 7. Basalt thickness estimates from craters with rims completely exposed on the maria. Craters that formed on maria and highlands are denoted by filled circles and triangles, respectively. The lunar maria basemap (gray) is from Nelson et al. (2014), and the basaltic unit boundaries (white) are from a compilation of previous studies (Hiesinger et al., 2006, 2011; Morota et al., 2009, 2011; Pasckert et al., 2018).

The largest source of uncertainty in our numerical inversions is by far related to the natural variability of the rim height of the initial fresh crater. We first quantified this by performing three inversions: one using the nominal initial topographic profile for fresh craters, and two using initial topographic profiles where the rim height was modified by the $\pm\sigma$ natural variability as quantified in section 5.2 and Table A3. The best fitting model parameters for these three cases were obtained using the procedure described above. Not surprisingly, the thickness of the mare basalts exterior to the crater for the two modified initial crater profiles differs with respect to that for the nominal profile by the uncertainty in the initial rim height.

After obtaining the best fitting parameters for the three initial topographic profiles, for each case we next used a simplified one-dimensional search to determine the uncertainties of the six model parameters. With the model parameters set to the best fitting values, the misfit was calculated by varying a single parameter. The 1 σ limits of this parameter were then defined as those values that could fit the observations to within a maximum allowable misfit. This maximum allowable misfit was defined as the global minimum found by the optimization toolbox plus the average standard error of the observed elevation profile. The standard error here is an estimate of how uncertain the mean elevation of the observed profile is at each radial distance, and the average standard error of the entire elevation profile of the selected 41 partially buried craters (see section 6) ranges from 1 to 6 m with a mean value of 3 m. We note that this technique for determining the limits of the parameters does not consider correlations with the other five parameters: quantifying such correlations by computing the full six-dimensional misfit function would be computationally demanding. Finally, we define the 1 σ limits for each parameter as the maximum and minimum 1 σ limits of the three inversions using the three separate initial crater profiles.

6. Mare Basalt Thickness Estimation Results

Before presenting the best fitting results, we first describe the details of a single representative inversion for the crater Seleucus (21.08°N, 66.67°W; D = 45.3 km; Figure 6a). This crater has a rim that is completely exposed and is located on the western margin of Oceanus Procellarum, and it was selected because it is one of the most degraded and best fitting craters in our crater database. Based on the best fit model parameters

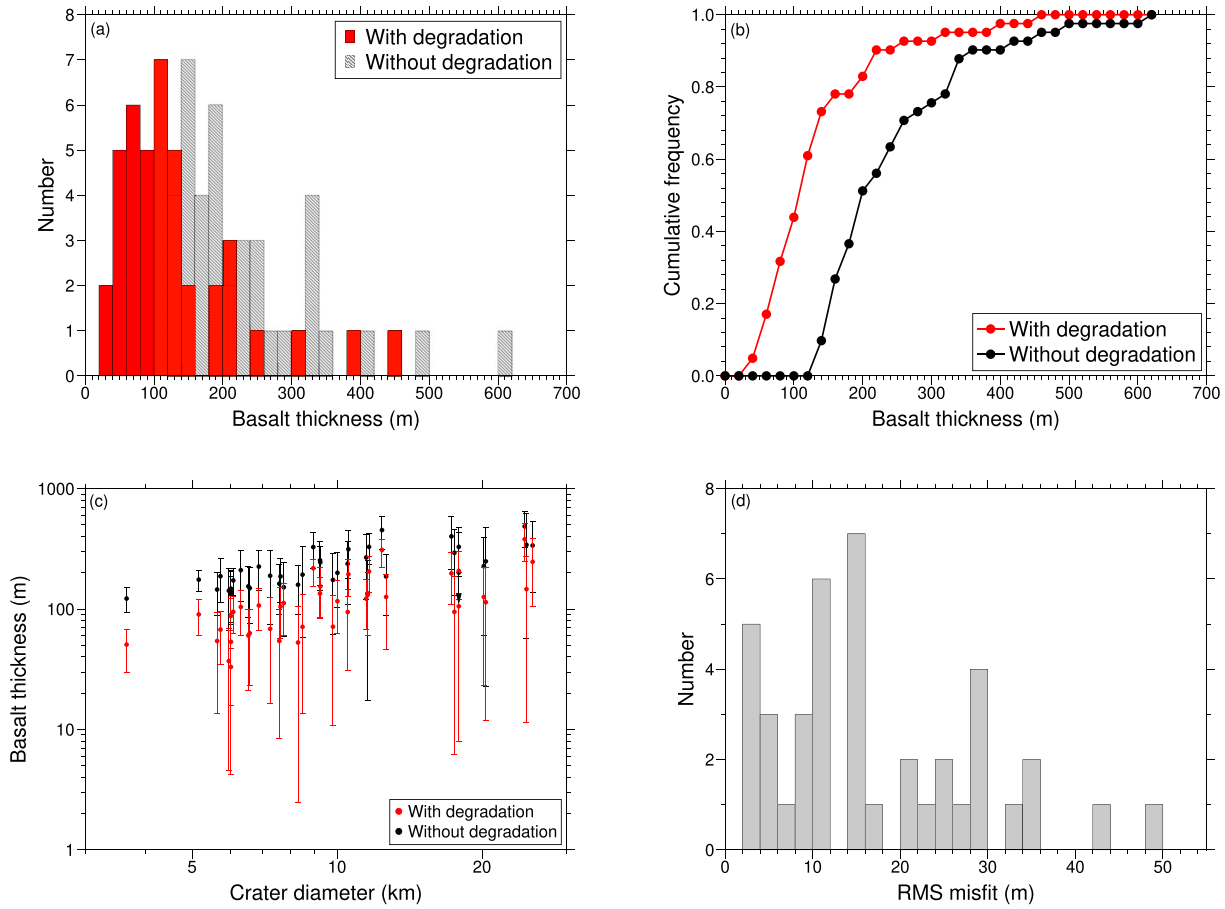

Figure 8. Histograms (a) and cumulative distributions (b) of basalt thicknesses with (red) and without (black) considering crater degradation. Basalt thicknesses as a function of crater diameter with (red) and without (black) considering the crater degradation process (c). Histogram of the root-mean-square (RMS) misfits between the modeled and observed profiles (d). The downward pointing arrow at 17.9 km in (c) indicates that the lower limit is 1 m.

determined by the crater degradation model, the history of Seleucus can be described as follows (Figures 6b and 7c). First, the crater formed on a highland target given that the FeO content of the exposed crater rim and proximal ejecta is about 12 wt.%. The initial crater diameter was 45.2 km with a rim height of 1,168 m (red), and given the crater size, it should have formed with a central peak. Between the times of crater formation and mare flooding, the crater rim height degraded by 73 m to 1,095 m (green). Then, mare basalts with a thickness of 455 $\pm$ 264 m erupted outside the crater rim partially flooding the crater ejecta, and mare basalts erupted inside the crater interior nearly completely burying the central peak. The crater profile then continued to erode to the present state, obtaining a rim height of 960 m with respect to the preflooding background. Thus, from crater formation to the present time, the rim was reduced in height by about 208 m. If rim erosion was not considered, the mare basalt thickness would be estimated to be 663 m, which is considerably larger than when considering crater degradation.

In this study, basalt thicknesses were estimated around 74 mare craters with rims completely exposed. Some of these craters either fit the observations poorly or had large uncertainties. Thus, we first discarded craters that had atypically high misfits (larger than 50 m). We then removed from further consideration craters where the 1 σ lower limit in the basalt thickness was equal to 0. In the end, we were left with 41 craters that were considered for further analyses, among which 16 formed on mare basement (circles) and 25 formed on highland basement (triangles; Figure 7). The crater diameters vary from 3.7 to 45.3 km, and the obtained basalt thicknesses range from a minimum of 33 m to a maximum of 455 m (Figures 8a–8c and Table A4). There is no clear pattern of the derived basalt thicknesses when plotted in map form. This is to be expected because two adjacent partially buried craters could have formed at different times and could have been embayed by different thicknesses of basaltic flows.

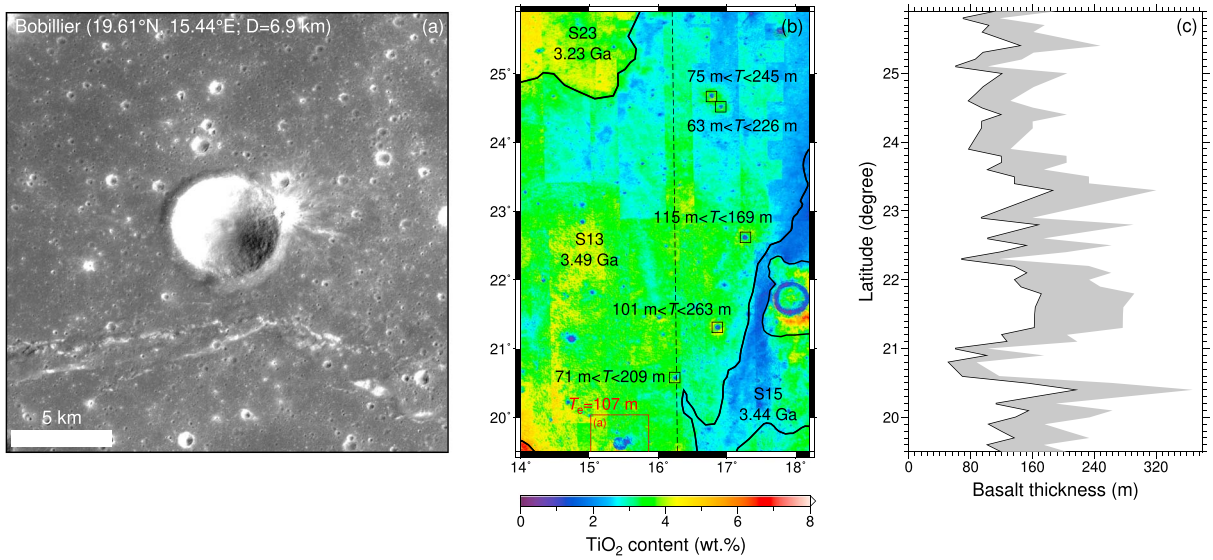

Figure 9. SELENE TC optical image (a) and SELENE MI-derived TiO_2 abundance map (b) near crater Bobillier (D = 6.9 km). In (b), the basalt thickness estimated from the crater degradation model surrounding the crater Bobillier is labeled in red, and those based on crater excavation depths are given in black (Ishiyama et al., 2013). Basaltic units are outlined in black and are labeled by the unit names and ages from Hiesinger et al. (2011). The ground track where SELENE LRS data (Data ID: LRS_SAR05KM_C_25N_016214E, LRS_SAR05KM_C_20N_016273E, and LRS_SAR05KM_C_15N_016329E) were obtained is denoted by the north-south dashed line. In (c), the calculated basalt thicknesses from the radar data are presented using a range of porosities from 0% to 45% where 0 porosity is denoted by the leftmost black line. SELENE TC = Selenological and Engineering Explorer Terrain Camera; MI = Multi-band Imager; LRS = Lunar Radar Sounder.

Figure 8c shows that there is a positive correlation between the estimated basalt thickness and crater diameter. This is simply because the crater rim height, which is the maximum thickness that can be retrieved from our method, increases with crater diameter (Pike, 1977). For the studied partially buried craters, the root-mean-square misfits (Figure 8d) between the best fitting and observed profiles are smaller than 50 m, with an average of 17 m. The initial crater diameter is found to be on average 95% of the observed value. The uncertainty in the basalt thickness is on average 67 m. The thicknesses of basalts in the interiors of 36 craters were also estimated, and these are 1,073 m on average (note that the crater floor is much deeper than the preflooding background).

If crater degradation was not included, these thicknesses would be considerably larger, ranging from 122 to 613 m. To be comparable with our obtained results, these results are based on the initial rim height-crater diameter ratio derived in this study instead of Pike (1977), and the initial rim height was estimated from the observed, present-day crater diameter. In this case, the median and average basalt thicknesses are 200 and 238 m, in comparison to the values of 105 and 130 m obtained when considering crater degradation. The ~100-m overestimate in the average basalt thickness when neglecting degradation is therefore about 25–50% of the average value (200–400 m) that was previously estimated by De Hon and Waskom (1976) and De Hon (1979).

7. Discussion

7.1. Comparisons With Other Techniques

In this section, we compare our estimated mare basalt thicknesses with other techniques, including crater excavation depths, radar sounding observations, lava flow front measurements, and gravity constraints.

In southern Mare Serenitatis, a partially buried crater named Bobillier (19.61°N, 15.44°E; D = 6.9 km) was identified (Figure 9a). For this crater, the TiO_2 content of the western and southern crater ejecta (>5 wt.%) is distinctly higher than that of the surface lava flow flooding the distal ejecta (3–4 wt.%; Figure 9b). Our simulation shows that the mare basalt emplaced on Bobillier's ejecta is 107 ± 41 m in thickness, which we interpret as corresponding to the thickness of the unit S13 (Hiesinger et al., 2011) in this image. Coincidently, in the same basaltic unit S13 five craters (black boxes) were identified by Ishiyama et al. (2013) with different TiO_2 contents (Figure 9b) in their ejecta. These craters penetrated through the surface unit and also excavated the underlying unit with higher TiO_2 concentrations. The diameters for these craters vary

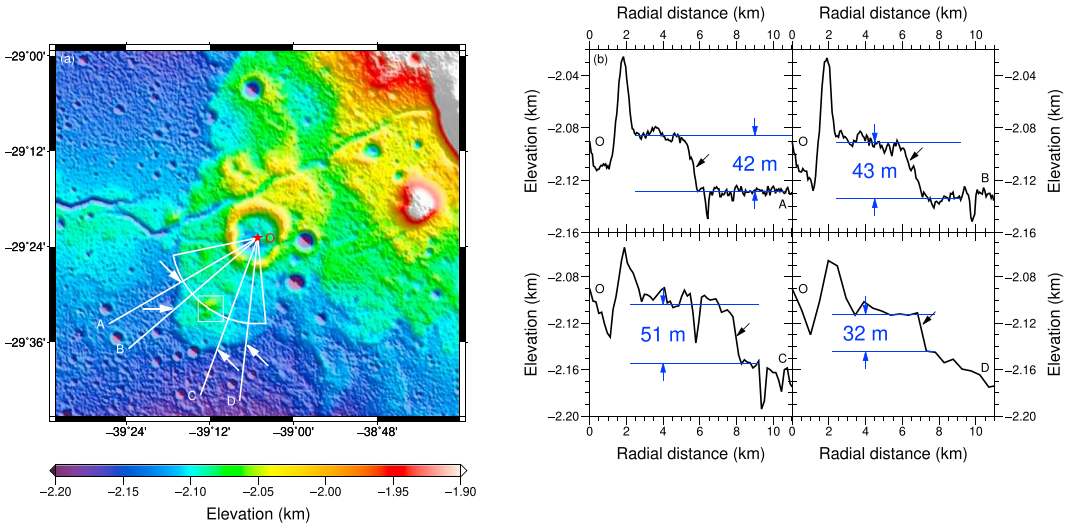

Figure 10. Elevation map of an unnamed partially buried crater (D = 3.6 km) (a). The red star indicates the crater center, the white fan is the region where the elevation profile was extracted when performing the inversion in section 5, the white arrows point to the lava flow fronts, and the white lines represent individual profiles OA, OB, OC, and OD. The elevation profiles are plotted in (b), where the black arrows point to the lava flow fronts, and the solid blue lines indicate the elevations above and below the lava flow fronts.

from 2.0 to 3.1 km, so the maximum basalt thickness of the overlying surface unit should be 169 to 263 m based on their crater excavation depths. The existence of small craters (0.8–1.4 km in diameter) that did not excavate the underlying lava flow places a minimum thickness of 71–115 m on the surface unit. Our derived thickness is 107 ± 41 m, which is consistent with the thickness range of 71–209 m given by the nearest crater pair to the partially buried crater (Figure 9b). We note that if crater degradation was not considered, the basalt thickness would be 225 m, which is larger than the upper bound of 209 m.

In the same region of the crater Bobillier, the SELENE LRS also detected subsurface reflectors (Ishiyama et al., 2013). We reanalyzed the SAR-processed radargram to derive basalt thickness along its track with latitudes from 19.5°N to 26°N (Figure 9c; see Text S3 in the supporting information for details). Along the ground track plotted in Figure 9b, continuous subsurface echoes are found from 19.5°N to 25.9°N. The subsurface reflectors were identified visually by the peaks in each individual observation as well as the lateral continuity in the radargram. The apparent depths were converted to true depths by using an estimate of the dielectric permittivity of the unit. For this, we made use of the FeO and TiO_2 contents as calculated from the MI data, and we assumed a range of porosities from 0% to 45%. Using the relations in Fa and Wieczorek (2012) that quantify permittivity as a function of composition and porosity, we estimate the depth of this reflector to be on average 120 to 161 m below the surface for porosities of 0–45%. Close to the crater Bobillier at (19.61°N, 16.33°E), the thickness given by radar observations is 104 m (porosity=0), which is consistent with our estimate value of 107 ± 41 m. We note that considering the range in basalt thicknesses estimated from the SELENE LRS along the ground track (~195 km long), there could be multiple flow units in this region.

The most direct estimation of the thickness of a lava flow is the measurement of lava flow front heights. On the northeastern floor of the crater Lee M, an unnamed partially buried crater (29.37°S, 39.09°W; D = 3.6 km) was identified (Figure 10a). This crater is embayed by a basaltic unit whose origin is to the northeast of the crater. Four radial topographic profiles were extracted, avoiding the topographic high to the southwest of the studied crater (white box Figure 10a). The front heights were measured from the elevation difference between the upper and lower lava flows, providing estimates of the flow front height of 42, 43, 51, and 32 m. Given the standard deviation in elevations of the surrounding plains and the lava flow, these estimates may have an uncertainty of about 8 m. Our estimated basalt thickness from the crater degradation model is 9 m with an upper limit of 29 m. This estimate is somewhat smaller than the lower limit of measured lava flow front heights. However, it should be noted that the about 40% variation of measured flow front heights may imply a natural variability of the basalt thickness in the region of this crater. We also note that if topographic degradation was not taken into account for this highly degraded crater, the basalt thickness would

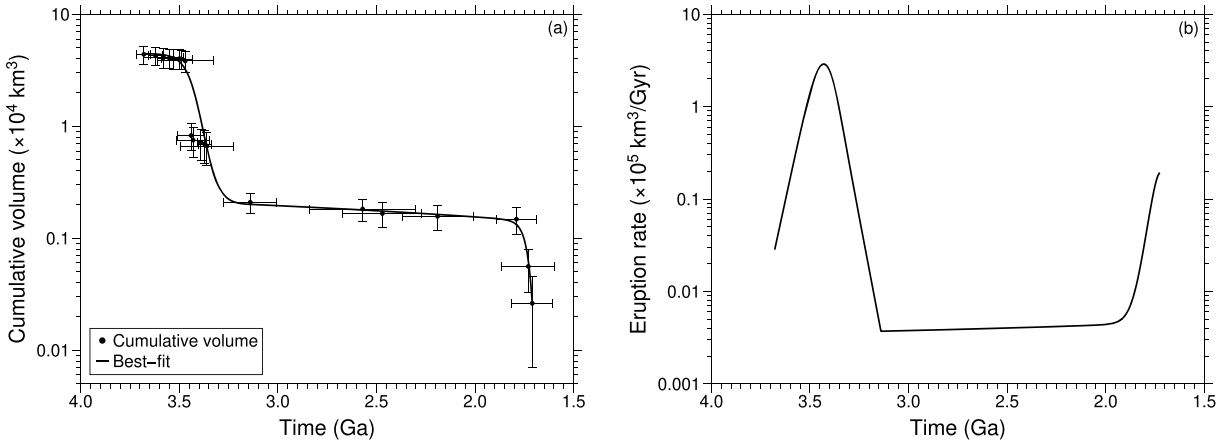

Figure 11. Cumulative volume of the mare basalts for surfaces with ages less than a given value (a) and eruption rate of the mare basalts (b) as a function of time. In (a), the cumulative volume V_c is fitted using a sigmoid-like function before 3.14 Ga: $\log(V_{c1}) = 1.35/(1 + \exp(-190.22 \times \log(t_1) + 100.63)) + 3.30$, and a sum of two exponential functions after 3.14 Ga: $\log(V_{c2}) = 3.03 \times \exp(0.18 \times \log(t_2)) - 2.49 \times 10^{14} \times \exp(-143.60 \times \log(t_2))$, where V_{c1} and V_{c2} are cumulative volume and t_1 and t_2 are time. The uncertainty for the cumulative volume is calculated using the uncertainty of the thickness of basaltic unit, and the uncertainty of the basalt age is taken from a compilation of previous studies (Hiesinger et al., 2006, 2011; Morota et al., 2009, 2011; Pasckert et al., 2018).

be 77 m, which is more inconsistent with the observations (average = 42 m) than ours that takes into account crater degradation.

Basalt thicknesses derived from gravity observations are of great interest because they represent the total thickness of lavas that erupted in the region. These estimates can be compared directly with our study only for craters that formed initially on a highland target: for these craters, the estimated basalt thicknesses correspond to the total thickness of lava flows in the region. A recent study of the lunar gravity field shows that the total basalt thickness on the western nearside maria (19°S–45°N, 68–8°W) is 740 m on average (Gong et al., 2016), with these estimates representing averages within a circle with a diameter of 425 km. As a comparison, our estimated total basalt thickness using only those craters that formed on highland crust ($N = 25$) is only 119 m on average. This discrepancy is largely a result of the fact that the craters that formed on highland basement in our study are mostly found near the mare-highland boundary, where we expect the basalt flows to be thinner than in the interior of the mare.

7.2. Cumulative Volume and Eruption Rates of Mare Basalts

With our estimates for the thickness of basaltic lava flows, it is possible to estimate the volume of the erupted basalts and their long-term eruption rate. Our craters sampled 23 of the basalt units mapped by a compilation of previous studies (Hiesinger et al., 2006, 2011; Morota et al., 2009, 2011; Pasckert et al., 2018), for which their surface ages vary from 1.7 to 3.7 Gyr with surface areas ranging from 1,429 to 95,727 km^2.

The cumulative volume of the sampled lava flows is plotted for all ages less than a given value in Figure 11a, showing that there is a total of 4.4×10^4 km^3 of lava that erupted from 3.7 to 1.7 Ga. The total cumulate volume that erupted on the Moon is of course greater than this, as our study did not sample all lava flow units, and there may be additional flows beneath the surficial flows we investigated. We can correct this effect approximately by using the average total thickness of mare basalts from the subset of mare craters that formed on highland basement (25 triangles in Figure 7) and using the known surface area of all basaltic flows. With an average total thickness of 119 m and the total surface area of mare basalts (6.2×10^6 km^2; Head, 1975), the resulting total volume is 7.4×10^5 km^3. As a comparison, the total basalt volume reported by previous studies varies from 1×10^6 to 1×10^7 km^3 (e.g., Budney & Lucey, 1998; Head & Wilson, 1992; Hörz, 1978). The discrepancy in estimates of total basalt volume is again due to the fact that the partially buried craters that formed on the highlands are preferentially located along mare margins where thinner lava flows are expected, whereas other studies used estimates of the basalt thickness in the mare centers that are considerably larger.

The eruption rate of mare basalts on the Moon can be calculated by taking the derivative of the best fitting cumulative volume (Figure 11b). The most prominent feature in this plot is a peak at 3.4 Ga with a value of 2.9×10^5 km^3/Gyr, followed by a rapid decline to 3.7×10^2 km^3/Gyr at 3.1 Ga. The major phase of basalt

eruption (3.7–3.1 Ga) in our study is consistent with thermal evolution models that take into account the asymmetric distribution of heat producing elements in the crust (Laneuville et al., 2013), where the main eruptive phase is found to lie between about 3.8 and 3.3 Ga. Then, the volcanic activity became less active until a secondary peak was reached at 1.7 Ga with a value of 1.9×10^4 km^3/Gyr, indicating a more recent, episodic eruption. Hiesinger et al. (2011) also estimated the eruption rate from the cumulative volume plot of mare basalts, by assuming a constant basalt thickness of 10–100 m and that all the basalts erupted at the age of the uppermost surface unit. Their pattern is similar to ours, which shows that the mare basalt flux was extremely low from 3.7 to 4.0 Ga, reached a peak at 3.5 Ga with a value of 5.0×10^4–4.3×10^5 km^3/Gyr, and then gradually decreased with time but slightly peaked at 2.1 Ga with a value of 2.5×10^4–1.0×10^5 km^3/Gyr.

Above, we calculated the average eruption rate of lavas on the Moon over geologic time, by averaging over many units of different ages and areas. The rate at which lava is extruded to the surface during an individual eruptive event is thus not important for our analysis, as it is expected to occur over a period of time that is extremely short in comparison to the duration of mare volcanism. Regardless, some studies have attempted to estimate the eruption rates for individual eruptive events by dividing the thickness of the basalt layer by the age difference between overlying and underlying layers (e.g., Oshigami et al., 2014; Weider et al., 2010). Their derived eruption rates should not be compared to the results in this study, as the two eruption rates correspond to two distinctly different geologic processes (i.e., how long it takes lava for a single event to reach the surface vs. how much lava is being eruptive over the entire lunar surface as a function of time).

7.3. Scale and Temporal Dependence of Crater Degradation

One of the outputs of our model is the product of diffusivity and time, both before the mare basalts erupted and embayed the crater and afterward. The ages of the basaltic surface units can be estimated using the crater chronology technique (e.g., Hiesinger et al., 2011; Morota et al., 2011), and using the ages of these flows, we can estimate the average diffusivity between the present day and when the lavas erupted. If we further assume that the diffusivity was the same before the crater was flooded, we can even estimate the age when the crater formed. In this section, we investigate the topographic diffusivity by examining its dependence on crater size, time, and target type (mare and highland).

The diameter dependence of topographic diffusivity has a strong theoretical basis (e.g., Howard, 2007; Minton et al., 2019; Soderblom, 1970; Xie et al., 2017). Soderblom (1970) was the first to investigate the crater degradation process by modeling the downslope movement of crater ejecta due to micrometeoroid bombardment. This approach used the assumption of mass conservation, where the net mass of ejecta materials moving into (out of) a volumetric unit must be equal to that accumulated (lost) in this unit per unit area and time. In this model, the topographic diffusivity is expressed as

$$\kappa = \frac{CAD_{\max}^{4-\lambda}}{4-\lambda} \tag{3}$$

where C is a constant related to the mass of the ejecta excavated by micrometeorite bombardment, A and λ are coefficients of the size-frequency distribution of the small craters that formed on the ejecta of parent crater ($N = AD^{-\lambda}$) where D is the diameter of the small craters (Shoemaker, 1965), and $D_{\max}$ is the maximum diameter of the small craters that diffusively erode the parent crater.

In this model, the maximum size of the crater diffusively eroding the host crater might be expected to scale with the host crater size. Previous studies proposed that a cutoff of 10% of the parent crater diameter would be an appropriate upper limit for the craters that erode the parent crater in a diffusive "sand blasting" way (Minton & Fassett, 2016). The power law coefficient λ is expected to be close to 3 (Shoemaker, 1965), implying that $\kappa = \kappa_0 D$, where D is the diameter of the parent crater with $D = 10 \times D_{\max}$ and κ_0 is a reference diffusivity at a diameter of 1 km (Xie et al., 2017). Though approximate, diffusivity might be expected to increase linearly with crater diameter.

Variations in the impact flux could also result in variations in the topographic diffusivity, primarily by changes in the parameter A. During the past 3 Gyr, the lunar impact flux is believed to have been relatively constant (e.g., Le Feuvre & Wieczorek, 2011; Neukum et al., 2001; Shoemaker, 1965). However, the flux is known to increase at earlier times, with the flux at 3.9 Ga being about 500 times the flux at 3 Ga (e.g., Neukum et al., 2001). Furthermore, the recent lunar impact flux could be modulated by the formation of asteroid families in the inner main belt such as the Flora and Baptistina asteroid families, which may have formed at 100 Ma and around 160 Ma, respectively (Bottke et al., 2008; Nesvorný et al., 2002).

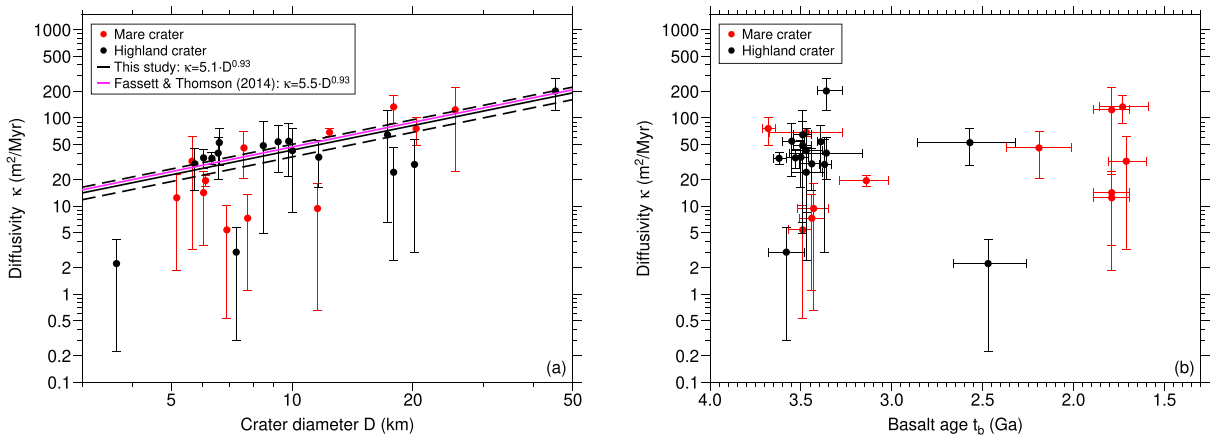

Figure 12. Diffusivity as a function of crater diameter (a) and basalt age (b). Craters that formed on mare and highland basements are shown in red and black, respectively. In (a), the solid and dashed black lines are the best fit ($\kappa = 5.1 \times D^{0.93}$) and 1 standard deviation uncertainty, respectively, and the magenta line is the best fit inferred from Fassett and Thomson (2014). In (b), the basalt ages and their error bars were taken from a compilation of previous studies (Hiesinger et al., 2006, 2011; Morota et al., 2009, 2011; Pasckert et al., 2018).

We examine the dependence of topographic diffusivity on crater diameter in Figure 12a. Though there is much scatter, the topographic diffusivity increases approximately linearly with crater diameter, as predicted by equation (3) and Xie et al. (2017). Fitting these data to a power law of the form $\kappa = \kappa_0 D^{\beta}$ provides a reference diffusivity of 5.1 ± 0.8 m^2/Myr with an exponent of 0.93 that is suggested by Xie et al. (2017). Fassett and Thomson (2014) investigated 13,657 small ($0.8 \leq D \leq 5$ km), unburied craters on lunar maria and determined κ_0 to be 5.5 m^2/Myr, which is close to our value. The diameter dependence of topographic diffusivity has also been strongly supported by the study of mare crater degradation ($0.8 \leq D \leq 5$ km) where larger craters were found to have larger topographic diffusivities (Fassett et al., 2018), and the modeling of topographic degradation of craters ($D \leq 100$ m) at the Apollo 15 landing site where smaller craters were thought to have smaller topographic diffusivities (Minton et al., 2019). The partially buried craters used in this study cover a larger diameter range ($3.7 \leq D \leq 45.3$ km), which strongly supports the diameter dependence of the diffusivity that both we and they found.

The topographic diffusivity as a function of the basalt age is plotted in Figure 12b to investigate how diffusivity depends on the impact flux. As can be seen, there is no significant correlation between the topographic diffusivity and the basalt age before and after 3 Ga. From a statistical point of view, the mean topographic diffusivities before and after 3 Ga are 52.1 ± 50.3 and 44.3 ± 42.7 m^2/Myr, respectively, implying that the older and younger topographic diffusivities are almost indistinguishable. We further performed a Kolmogorov-Smirnov test on these two groups of topographic diffusivities, which can help to examine if they are sampled from the same population or not (Massey, 1951). A null hypothesis indicates that the two distributions are drawn from the same population, and the P value significance level is commonly set to be 0.05 (Robbins et al., 2014). The calculated P value of 0.96 is much larger than this significance level, which means the null hypothesis cannot be rejected. In other words, there is no evidence for temporal variations in the topographic diffusivity in our data set. Fassett and Thomson (2014) suggested that the topographic diffusivity before 3 Ga was higher than that after 3 Ga. However, it should be noted that the diameter range of craters investigated in Fassett and Thomson (2014) varies by a factor of six, and the largest craters are found to be greater in age and have larger diffusivities. Therefore, the increasing topographic diffusivity before 3 Ga in Fassett and Thomson (2014) could be biased by the inclusion of the largest and oldest craters in their study, which are expected to have the highest diffusivities.

It is difficult to constrain the effect of target properties on diffusivity as equation (3) has no dependence on target properties. Nevertheless, we might expect highland terrain to be more fractured than the mare (e.g., Hartmann, 1973; Kreslavsky & Head, 2016) and that this would increase the rate of impact crater degradation in the highlands. We investigated whether the diffusivity is different for craters that formed on mare and highland targets. The topographic diffusivities for mare and highland craters were fitted using a power law function with the same exponent of 0.93, and we found that the reference diffusivities (5.5 ± 1.6 m^2/Myr vs.

4.8 ± 1.0 m^2/Myr) were almost the same. This suggests that highland and mare craters should degrade at a similar rate.

8. Conclusions

A global database of buried craters was constructed in this study using newly acquired remote sensing data sets. The identified buried craters were classified into three classes including craters with rims completely exposed, those with rims partially exposed, and those with rims completely buried. The spatial distribution and size-frequency distributions of these buried craters show that partially buried craters preferentially occur along mare-highland boundaries where the basalt thickness is expected to be thinner than in the central mare. A new elevation model for lunar fresh craters was constructed, and numerical modeling of the crater degradation process was then performed to estimate the thickness of mare basalts that embay the partially buried craters. Our overall results show that the obtained basalt thicknesses vary from 33 to 455 m and are significantly thinner than those obtained without considering the crater degradation process (a reduction of 95 m in median value). For selected craters, we demonstrated that the obtained basalt thicknesses were consistent with other estimates obtained from crater excavation depths and sounding radar observations, and comparable to those obtained from lava flow front height measurements. The estimated eruption rate of lunar mare basalts peaked at 3.4 Ga and then deceased with time, indicative of gradual cooling of the lunar interior. The best fitting topographic diffusivity increases linearly with crater diameter and does not vary with time and terrain type, implying that the crater degradation process is scale dependent.

Although our work has improved upon previous studies that used partially buried craters to investigate mare basalt thicknesses, we have identified a number of complicating factors that should be addressed in future studies. As an example, we employed a simple axisymmetric model for the topographic degradation and lava emplacement. This model, however, cannot account for partially buried craters on the mare-highland boundary or for mare craters where a portion of the rim was breached. Second, our results show considerable scatter in how topographic diffusivity varies with crater size. A portion of this scatter may be related to our use of axisymmetric crater profiles, and the assumption of a uniform lava thickness surrounding the crater. Third, although the initial crater profile for simple craters is well constrained, the initial crater shapes for transitional and complex craters have considerable variability. Finally, our work did not consider the contribution from nondiffusive processes that might be important for some craters.

The method of using partially buried craters to estimate lava flow thicknesses can be easily applied to Mercury, where crater degradation processes are similar to those on the Moon. Previous studies (e.g., Head et al., 2011; Ostrach et al., 2015) did not consider the effect of crater degradation, and crater degradation on Mercury could be twice as important as on the Moon (Fassett et al., 2017). Therefore, larger biases would be expected for this planet if lava flow thickness estimates did not consider crater degradation. Our model could conceivably be applied to Mars, but for this planet, both diffusive (e.g., micrometeorite bombardment, mass wasting, rain splash, and solifluction) and nondiffusive (e.g., fluvial events) topographic degradation processes need to be considered, and the latter plays an important role during the Noachian period (Craddock & Howard, 2002; Craddock et al., 1997, 2018).

Appendix A: Initial Crater Profile Modeling

Our derived shape profiles for fresh craters are presented in Tables A1 and A2. Table A1 provides the generic mathematical forms used to reconstruct the profile, whereas Table A2 provides relevant constants, and morphometric relations for the central peak radius (R_{cp}), central peak height (h_{cp}), crater floor radius (R_{cf}), crater depth (d_{cf}), rim height (h_r), and continuous ejecta radius (R_e). The coefficients a–f that are required in Table A1 can be numerically determined by setting the function equal to the known values at the relevant tie points. All the vertical parameters (h_{cp}, d_{cf}, and h_r) are normalized by crater diameter, and all the radial parameters (r, R_{cp}, R_{cf}, and R_e) are normalized by crater radius. Additional details can be found in the supporting information.

Table A3 presents the natural variability in the rim height for fresh craters of several bin sizes. The natural variability is defined as the root-mean-square deviation of the rim heights with respect to the best fitting functions provided in Table A2. In this tabulation, highland and mare craters were combined into a single

Table A1
Mathematic Forms for Fresh Lunar Impact Craters

Morphology	Target type	Elevation profile	Range
Simple	Mare	-0.165	$r \le 0.2$
($1 < D \le 15$ km)		$-0.292r^3 + 0.489r^2 + 0.028r - 0.188$	$0.2 < r \le 1$
		$-0.081r^3 + 0.419r^2 - 0.731r + 0.430$	$1 < r \le 1.7$
		0	$r > 1.7$
	Highland	-0.176	$r \le 0.2$
		$-0.400r^3 + 0.693r^2 - 0.0727r - 0.186$	$0.2 < r \le 1$
		$-0.0577r^3 + 0.312r^2 - 0.567r + 0.348$	$1 < r \le 1.8$
		0	$r > 1.8$
Transitional	Mare and highland	$h_r - d_{cf}$	$r \le R_{cf}$
($15 < D \le 20$ km)		$\exp(cr) + d$	$R_{cf} < r \le 1$
		$\exp(er) + f$	$1 < r \le R_e$
		0	$r > R_e$
Complex	Mare and highland	$\exp(ar) + b$	$r \le R_{cp}$
($D > 20$ km)		$h_r - d_{cf}$	$R_{cp} < r \le R_{cf}$
		$\exp(cr) + d$	$R_{cf} < r \le 1$
		$\exp(er) + f$	$1 < r \le R_e$
		0	$r > R_e$

Table A2
Morphometric Parameters of Fresh Transitional and Complex Craters

Morphology	Target type	Parameter
Transitional	Mare	$h_r = 0.191D^{-0.606}$
($15 < D \le 20$ km)		$d_{cf} = 191D^{-2.53}$
		$R_{cf} = -10.7D^{-1.30} + 0.522$
		$R_e = 2.26$
	Highland	$h_r = 0.0346D^{-0.001}$
		$d_{cf} = 15.1D^{-1.58}$
		$R_{cf} = -2.30D^{-0.637} + 0.609$
		$R_e = 1.91$
Complex	Mare	$h_r = 0.139D^{-0.500}$
($D > 20$ km)		$d_{cf} = 0.437D^{-0.500}$
		$R_{cf} = -10.7D^{-1.30} + 0.522$
		$R_e = 2.26$
		$h_{cp} = -3.56 \times 10^{-5}D^2 + 0.00290D - 0.0438$ ($20 < D \le 40$ km)
		$h_{cp} = -3.65 \times 10^{-6}D^2 + 4.47 \times 10^{-4}D + 0.00330$ ($40 < D < 100$ km)
		$R_{cp} = -3.18 \times 10^{3}D^{-3.12} + 0.280$ ($20 < D \le 40$ km)
		$R_{cp} = -3.80 \times 10^{-4}D + 0.263$ ($40 < D < 100$ km)
	Highland	$h_r = 0.101D^{-0.358}$
		$d_{cf} = 1.01D^{-0.674}$
		$R_{cf} = -2.30D^{-0.637} + 0.609$
		$R_e = 1.91$
		$h_{cp} = -2.48 \times 10^{-5}D^2 + 0.00234D - 0.0368$ ($20 < D \le 50$ km)
		$h_{cp} = -5.04 \times 10^{-5}D + 0.0208$ ($50 < D < 140$ km)
		$R_{cp} = -7.07 \times 10^{3}D^{-3.42} + 0.252$ ($20 < D \le 50$ km)
		$R_{cp} = -3.44 \times 10^{-4}D + 0.258$ ($50 < D < 140$ km)

Note. Vertical parameters are scaled by crater diameter, whereas horizontal parameters are scaled by crater radius.

Table A3
Natural Variability in the Initial Rim Height As a Function of Crater Diameter

Crater diameter bin (km)	N	Initial rim height variability (m)
$1 \leq D \leq 5$	6	17
$5 < D \leq 10$	9	24
$10 < D \leq 15$	8	73
$15 < D \leq 20$	13	125
$20 < D \leq 35$	9	130
$35 < D \leq 50$	7	271

Table A4
Basalt Thickness Estimates Surrounding Partially Buried Craters

Number	Flag	D (km)	Longitude (°)	Latitude (°)	T_{ext} (m)	T_{ext}^{min} (m)	T_{ext}^{max} (m)
1	0	2.2	38.34	14.64	16	0	35
2	0	2.5	−28.45	40.94	4	0	14
3	0	3.4	−47.50	30.90	2	0	21
4	0	3.4	−41.02	−2.66	22	0	40
5	0	3.6	−39.09	−29.37	9	0	29
6	1	3.7	−53.60	−4.96	51	30	67
7	0	3.8	−58.16	−6.35	2	0	23
8	0	3.8	−31.50	22.24	18	0	39
9	1	5.2	−58.86	26.63	90	60	121
10	0	5.3	38.47	14.35	20	0	52
11	1	5.6	−56.28	16.49	54	14	93
12	1	5.7	−54.24	47.56	67	35	96
13	1	6.0	104.25	25.33	37	5	69
14	1	6.0	−26.31	54.69	33	4	67
15	1	6.0	−59.96	27.78	88	47	122
16	1	6.0	162.44	−33.23	53	16	91
17	1	6.1	−31.17	5.87	95	62	127
18	0	6.2	−19.86	45.54	44	0	78
19	1	6.3	86.38	17.23	104	60	143
20	0	6.3	26.28	14.08	33	0	64
21	1	6.5	53.65	2.37	60	21	100
22	1	6.6	149.91	26.23	63	23	99
23	0	6.8	28.41	11.34	7	0	45
24	1	6.9	15.44	19.61	107	66	148
25	0	7.2	172.75	−17.63	33	0	73
26	1	7.3	58.37	−0.86	69	16	125
27	0	7.3	−60.10	28.96	4	0	47
28	0	7.5	29.31	14.81	2	0	47
29	1	7.6	−44.71	1.14	54	8	99
30	1	7.6	−43.57	4.63	105	57	151
31	1	7.8	−62.04	50.10	112	60	161
32	1	8.3	36.92	35.46	53	2	105
33	1	8.5	147.35	28.74	71	14	133
34	0	8.9	29.19	16.22	29	0	86
35	1	8.9	37.88	12.06	218	154	259
36	0	9.0	144.66	26.84	56	0	106
37	1	9.2	22.94	39.05	135	84	183

Table A4 *Continued*

Number	Flag	D (km)	Longitude (°)	Latitude (°)	T_{ext} (m)	T_{ext}^{min} (m)	T_{ext}^{max} (m)
38	1	9.2	−159.65	−36.24	154	85	220
39	1	9.8	−9.45	27.37	71	11	130
40	1	10.0	-29.48	−0.64	116	63	172
41	1	10.5	-52.28	53.61	95	31	145
42	1	10.6	59.44	−2.16	195	127	258
43	1	11.5	-75.61	17.77	122	68	177
44	1	11.6	-42.99	−7.88	131	61	200
45	1	11.7	159.62	−51.40	205	136	276
46	1	12.4	50.44	−6.96	310	220	378
47	1	12.6	70.95	−50.16	126	46	195
48	0	13.5	−23.00	61.90	65	0	148
49	1	17.3	146.66	27.45	198	110	296
50	1	17.5	61.78	−17.58	95	6	188
51	1	17.9	−46.57	21.66	208	120	301
52	1	17.9	−29.20	−1.48	105	8	201
53	1	20.2	177.42	−36.73	126	23	223
54	1	20.4	20.11	10.49	114	12	220
55	1	24.5	−23.13	40.41	380	249	512
56	1	24.7	−31.91	−32.97	146	11	276
57	1	25.5	-58.79	23.38	247	104	384
58	1	45.3	-66.67	21.08	455	193	720

Note. D is the observed, final crater diameter. T_{ext} is the best fitting exterior basalt thickness, and T_{ext}^{min} and T_{ext}^{max} are its lower and upper bounds. The variable Flag is set to zero whenever the minimum basalt thickness is consistent with being zero. Only craters with Flag equal to 1 are considered for further analysis in the text.

database to improve the statistics, but it was found that the variabilities of the two separate classes were nearly the same.

Table A4 shows the final inversion results of the 58, well-fitted craters on maria with rims completely exposed. For simplicity, we only provide the crater diameter, coordinate, basalt thickness and its uncertainty here. For a more complete version with all the parameters and auxiliary information, the reader is referred to the attached long table in the supporting information.

Acknowledgments
We thank Rossman P. Irwin III, Jon C. Cawley, and Robert A. Craddock for helpful comments on the manuscript. We also thank C. I. Fassett, R. A. De Hon, and M. Lemelin for helpful discussions. This work was supported partly by the National Natural Science Foundation of China (11573005, 41941002), the CAS Key Laboratory of Lunar and Deep Space Exploration Grant (LDSE201704), the Science and Technology Development Fund of Macau (043/2016/A2), the French Space Agency (CNES), and the China Scholarship Council doctoral fellowship (201606010077). According to the FAIR Data principles, the authors declare the following Data Availability Statement: The Clementine UVVIS data and the SLDEM data can be acquired from the USGS Astrogeology Science Center (https://astrogeology.usgs.gov/search/map/Moon), the LRO LOLA and LROC data can be obtained from the NASA PDS Geosciences (http://pds-geosciences.wustl.edu/missions/lro/default.htm), and the SELENE TC, MI, and LRS data can be downloaded from the JAXA data archive webpage (https://darts.isas.jaxa.jp/planet/pdap/selene/). Anyone can download the data for free and without any licenses but sometimes needs to be registered as a user (USGS Astrogeology Science Center). The database of partially buried craters and the obtained basalt thickness estimates can be found in the supporting information. Figures were created using the Generic Mapping Tools (Wessel & Smith, 1991). This is PKU PRSL contribution 11.

References

Aeronautical Chart Information Center (1973). The lunar cartographic dossier: Lunar Astronautical Chart (LAC) series. https://www.lpi.usra.edu/resources/mapcatalog/LAC/lac_reference.pdf

Baldwin, R. B. (1949). *The face of the Moon*. Chicago: University of Chicago Press.

Baldwin, R. B. (1963). *The measure of the Moon*. Chicago: University of Chicago Press.

Baldwin, R. B. (1970). A new method of determining the depth of the lava in lunar maria. *Publications of the Astronomical Society of the Pacific*, *82*(488), 857–864. https://doi.org/10.1086/128974

Barker, M. K., Mazarico, E., Neumann, G. A., Zuber, M. T., Haruyama, J., & Smith, D. E. (2016). A new lunar digital elevation model from the Lunar Orbiter Laser Altimeter and SELENE terrain camera. *Icarus*, *273*, 346–355. https://doi.org/10.1016/j.icarus.2015.07.039

Basilevsky, A. T. (1976). On the evolution rate of small lunar craters. In *The 7th Lunar and Planetary Science Conference*, pp. 1005–1020.

Bell, J. F., & Hawke, B. R. (1984). Lunar dark-haloed impact craters: Origin and implications for Early Mare volcanism. *Journal of Geophysical Research*, *89*(B8), 6899–6910. https://doi.org/10.1029/JB089iB08p06899

Bottke, W. F., Levison, H., & Morbidelli, A. (2008). Understanding the impact flux on the Moon over the last 4.6 Gy. In *Workshop on the Early Solar System Impact Bombardment*, pp. 3005.

Braden, S. E., Stopar, J. D., Robinson, M. S., Lawrence, S. J., & van der Bogert, C. H. (2014). Evidence for basaltic volcanism on the Moon within the past 100 million years. *Nature Geoscience*, *7*(11), 787–791. https://doi.org/10.1038/NGEO2252

Budney, C. J., & Lucey, P. G. (1998). Basalt thickness in Mare Humorum: The crater excavation method. *Journal of Geophysical Research*, *103*(E7), 16,855–16,870. https://doi.org/10.1029/98JE01602

Cooper, B. L., Carter, J. L., & Sapp, C. A. (1994). New evidence for graben origin of Oceanus Procellarum from lunar sounder optical imagery. *Journal of Geophysical Research*, *99*(E2), 3799–3812. https://doi.org/10.1029/93JE03096

Cooper, M. R., Kovach, R. L., & Watkins, J. S. (1974). Lunar near-surface structure. *Reviews of Geophysics*, *12*(3), 291–308. https://doi.org/10.1029/RG012i003p00291

Craddock, R. A., Bandeira, L., & Howard, A. D. (2018). An assessment of regional variations in Martian modified impact crater morphology. *Journal of Geophysical Research: Planets*, *123*, 763–779. https://doi.org/10.1002/2017JE005412

Craddock, R. A., & Howard, A. D. (2000). Simulated degradation of lunar impact craters and a new method for age dating farside mare deposits. *Journal of Geophysical Research*, *105*(E8), 20,387–20,401. https://doi.org/10.1029/1999JE001099

Craddock, R. A., & Howard, A. D. (2002). The case for rainfall on a warm, wet early Mars. *Journal of Geophysical Research*, *107*(E11), 5111. https://doi.org/10.1029/2001JE001505

Craddock, R. A., Maxwell, T. A., & Howard, A. D. (1997). Crater morphometry and modification in the Sinus Sabaeus and Margaritifer Sinus regions of Mars. *Journal of Geophysical Research*, *102*(E6), 13,321–13,340. https://doi.org/10.1029/97JE01084

Croft, S. K. (1980). Cratering flow fields—Implications for the excavation and transient expansion stages of crater formation. In *The 11th Lunar and Planetary Science Conference*, pp. 2347–2378.

Culling, W. E. H. (1960). Analytical theory of erosion. *Journal of Geology*, *68*(3), 336–344. https://doi.org/10.1086/626663

Culling, W. E. H. (1963). Soil creep and the development of hillside slopes. *Journal of Geology*, *71*(2), 127–161. https://doi.org/10.1086/626891

De Hon, R. A. (1974). Thickness of mare material in the Tranquillitatis and Nectaris basins. In *The 5th Lunar and Planetary Science Conference*, pp. 53–59.

De Hon, R. A. (1979). Thickness of western mare basalts. In *The 10th Lunar and Planetary Science Conference*, pp. 274–276.

De Hon, R. A., & Waskom, J. D. (1976). Geologic structure of the eastern mare basins. In *The 7th Lunar and Planetary Science Conference*, pp. 2729–2746.

Defense Mapping Agency Topographic Center (1973). The Lunar Cartographic Dossier: Lunar Topographic Orthophotomap (LTO) and Lunar Orthophotmap (LO) series. https://www.lpi.usra.edu/resources/mapcatalog/LTO/lto_references.pdf

Eggleton, R. E. (1961). Thickness of the Apenninian series in the Lansberg region of the Moon (*Astrogeology Studies Annual Progress Report*). (pp. 19–31). Flagstaff: U. S. Geological Survey.

Eliason, E. M., McEwen, A. S., Robinson, M. S., Lee, E. M., Becker, T., Gaddis, L., et al. (1999). Digital processing for a global multispectral map of the Moon from the Clementine UVVIS imaging instrument. In *The 30th Lunar and Planetary Science Conference*, pp. 1933.

Evans, A. J., Andrews-Hanna, J. C., Head, J. W. III, Soderblom, J. M., Solomon, S. C., & Zuber, M. T. (2018). Re-examination of early lunar chronology with GRAIL data: Terranes, basins, and impact fluxes. *Journal of Geophysical Research: Planets*, *123*, 1596–1617. https://doi.org/10.1029/2017JE005421

Evans, A. J., Soderblom, J. M., Andrews-Hanna, J. C., Solomon, S. C., & Zuber, M. T. (2016). Identification of buried lunar impact craters from GRAIL data and implications for the nearside maria. *Geophysical Research Letters*, *43*, 2445–2455. https://doi.org/10.1002/2015GL067394

Fa, W., Liu, T., Zhu, M.-H., & Haruyama, J. (2014). Regolith thickness over Sinus Iridum: Results from morphology and size-frequency distribution of small impact craters. *Journal of Geophysical Research: Planets*, *119*, 1914–1935. https://doi.org/10.1002/2013JE004604

Fa, W., & Wieczorek, M. A. (2012). Regolith thickness over the lunar nearside: Results from Earth-based 70-cm Arecibo radar observations. *Icarus*, *218*(2), 771–787. https://doi.org/10.1016/j.icarus.2012.01.010

Fassett, C. I. (2016). Analysis of impact crater populations and the geochronology of planetary surfaces in the inner solar system. *Journal of Geophysical Research: Planets*, *121*, 1900–1926. https://doi.org/10.1002/2016JE005094

Fassett, C. I., Crowley, M. C., Leight, C., Dyar, M. D., Minton, D. A., Hirabayashi, M., et al. (2017). Evidence for rapid topographic evolution and crater degradation on Mercury from simple crater morphometry. *Geophysical Research Letters*, *44*, 5326–5335. https://doi.org/10.1002/2017GL073769

Fassett, C. I., Minton, D. A., Thomson, B. J., Hirabayashi, M., & Watters, W. A. (2018). Re-analysis of observations of crater degradation on the lunar maria accounting for anomalous diffusion. In *The 49th Lunar and Planetary Science Conference*, pp. 1502.

Fassett, C. I., & Thomson, B. J. (2014). Crater degradation on the lunar maria: Topographic diffusion and the rate of erosion on the Moon. *Journal of Geophysical Research: Planets*, *119*, 2255–2271. https://doi.org/10.1002/2014JE004698

Gifford, A. W., & El-Baz, F. (1981). Thicknesses of lunar mare flow fronts. *The Moon and the Planets*, *24*(4), 391–398. https://doi.org/10.1007/BF00896904

Gong, S., Wieczorek, M. A., Nimmo, F., Kiefer, W. S., Head, J. W., Huang, C., et al. (2016). Thicknesses of mare basalts on the Moon from gravity and topography. *Journal of Geophysical Research: Planets*, *121*, 854–870. https://doi.org/10.1002/2016JE005008

Hartmann, W. K. (1973). Ancient lunar mega-regolith and subsurface structure. *Icarus*, *18*, 634–636. https://doi.org/10.1016/0019-1035(73)90066-3

Haruyama, J., Hara, S., Hioki, K., Iwasaki, A., Morota, T., Ohtake, M., et al. (2012). Lunar global digital terrain model dataset produced from SELENE (Kaguya) terrain camera stereo observations. In *The 43rd Lunar and Planetary Science Conference*, pp. 1200.

Hawke, B. R., Blewett, D. T., Lucey, P. G., Smith, G. A., Bell, J. F. III, Campbell, B. A., & Robinson, M. S. (2004). The origin of lunar crater rays. *Icarus*, *170*(1), 1–16. https://doi.org/10.1016/j.icarus.2004.02.013

Head, J. W. (1975). Lunar mare deposits: Areas, volumes, sequence, and implication for melting in source areas. In *Conference on Origins of Mare Basalts and their Implications for Lunar Evolution*, pp. 66–69.

Head, J. W. (1976). Lunar volcanism in space and time. *Reviews of Geophysics*, *14*(2), 265–300. https://doi.org/10.1029/RG014i002p00265

Head, J. W. (1982). Lava flooding of ancient planetary crusts: Geometry, thickness, and volumes of flooded lunar impact basins. *Earth, Moon, and Planets*, *26*(1), 61–88. https://doi.org/10.1007/BF00941369

Head, J. W., Chapman, C. R., Strom, R. G., Fassett, C. I., Denevi, B. W., Blewett, D. T., et al. (2011). Flood volcanism in the northern high latitudes of Mercury revealed by MESSENGER. *Science*, *333*(6051), 1853–1856. https://doi.org/10.1126/science.1211997

Head, J. W., & Wilson, L. (1992). Lunar mare volcanism: Stratigraphy, eruption conditions, and the evolution of secondary crusts. *Geochimica et Cosmochimica Acta*, *56*(6), 2155–2175. https://doi.org/10.1016/0016-7037(92)90183-J

Head, J. W., & Wilson, L. (2017). Generation, ascent and eruption of magma on the Moon: New insights into source depths, magma supply, intrusions and effusive/explosive eruptions (Part 2: Predicted emplacement processes and observations). *Icarus*, *283*, 176–223. https://doi.org/10.1016/j.icarus.2016.05.031

Heiken, G. H., Vaniman, D. T., & French, B. M. (1991). *Lunar source book: A user's guide to the Moon*. New York: Cambridge University Press.

Hiesinger, H., Head, J. W., Wolf, U., Jaumann, R., & Neukum, G. (2002). Lunar mare basalt flow units: Thicknesses determined from crater size-frequency distributions. *Geophysical Research Letters*, *29*(8), 1248. https://doi.org/10.1029/2002GL014847

Hiesinger, H., Head, J. W., Wolf, U., Jaumann, R., & Neukum, G. (2006). New ages for basalts in Mare Fecunditatis based on crater size-frequency measurements. In *The 37th Lunar and Planetary Science Conference*, pp. 1151.

Hiesinger, H., Head, J. W., Wolf, U., Jaumann, R., & Neukum, G. (2011). Ages and stratigraphy of lunar mare basalts: A synthesis. *Geological Society of America Special Papers*, *477*, 1–51. https://doi.org/10.1130/2011.2477(01)

Hörz, F. (1978). How thick are lunar mare basalts. In *The 9th Lunar and Planetary Science Conference*, pp. 3311–3331.
Howard, A. D. (2007). Simulating the development of Martian highland landscapes through the interaction of impact cratering, fluvial erosion, and variable hydrologic forcing. *Geomorphology*, *91*(3-4), 332–363. https://doi.org/10.1016/j.geomorph.2007.04.017
Ishiyama, K., Kumamoto, A., Ono, T., Yamaguchi, Y., Haruyama, J., Ohtake, M., et al. (2013). Estimation of the permittivity and porosity of the lunar uppermost basalt layer based on observations of impact craters by SELENE. *Journal of Geophysical Research: Planets*, *118*, 1453–1467. https://doi.org/10.1002/jgre.20102
Kobayashi, T., Kim, J.-H., Lee, S. R., Kumamoto, A., Nakagawa, H., Oshigami, S., et al. (2012). Synthetic aperture radar processing of Kaguya Lunar Radar Sounder data for lunar subsurface imaging. *IEEE Transactions on Geoscience and Remote Sensing*, *50*(6), 2161–2174. https://doi.org/10.1109/TGRS.2011.2171349
Kreslavsky, M. A., & Head, J. W. (2016). The steepest slopes on the Moon from Lunar Orbiter Laser Altimeter (LOLA) data: Spatial distribution and correlation with geologic features. *Icarus*, *273*, 329–336. https://doi.org/10.1016/j.icarus.2016.02.036
Laneuville, M., Wieczorek, M. A., Breuer, D., & Tosi, N. (2013). Asymmetric thermal evolution of the Moon. *Journal of Geophysical Research: Planets*, *118*, 1435–1452. https://doi.org/10.1002/jgre.20103
Le Feuvre, M., & Wieczorek, M. A. (2011). Nonuniform cratering of the Moon and a revised crater chronology of the inner solar system. *Icarus*, *214*(1), 1–20. https://doi.org/10.1016/j.icarus.2011.03.010
Lemelin, M., Lucey, P. G., Gaddis, L. R., Hare, T., & Ohtake, M. (2016). Global map products from the Kaguya Multiband Imager at 512 ppd: Minerals, FeO, and OMAT. In *The 47th Lunar and Planetary Science Conference*, pp. 2994.
Li, C., Xing, S., Lauro, S. E., Su, Y., Dai, S., Feng, J., et al. (2018). Pitfalls in GPR data interpretation: False reflectors detected in lunar radar cross sections by Chang'E-3. *IEEE Transactions on Geoscience and Remote Sensing*, *56*(3), 1325–1335. https://doi.org/10.1109/TGRS.2017.2761881
Lucey, P. G., Blewett, D. T., & Jolliff, B. L. (2000). Lunar iron and titanium abundance algorithms based on final processing of Clementine ultraviolet-visible images. *Journal of Geophysical Research*, *105*, 20,297–20,305. https://doi.org/10.1029/1999JE001117
Marshall, C. H. (1963). Thickness and structure of the Procellarian system in the Lansberg Region of the Moon (*Astrogeology Studies Annual Progress Report*). (pp. 12–18). Flagstaff: U. S. Geological Survey.
Massey, F. J. (1951). The Kolmogorov-Smirnov test for goodness of fit. *Journal of the American Statistical Association*, *46*(253), 68–78. https://doi.org/10.2307/2280095
MathWorks Inc (2017). Global optimization toolbox: MATLAB documentation. https://www.mathworks.com/help/gads/index.html
Melosh, H. J. (1989). *Impact cratering: A geologic process*. New York: Oxford University Press.
Melosh, H. J. (2011). *Planetary Surface Processes*. New York: Cambridge University Press.
Michaut, C., & Pinel, V. (2018). Magma ascent and eruption triggered by cratering on the Moon. *Geophysical Research Letters*, *45*, 6408–6416. https://doi.org/10.1029/2018GL078150
Minton, D. A., & Fassett, C. I. (2016). Crater equilibrium as an anomalous diffusion process. In *The 47th Lunar and Planetary Science Conference*, pp. 2623.
Minton, D. A., Fassett, C. I., Hirabayashi, M., Howl, B. A., & Richardson, J. E. (2019). The equilibrium size-frequency distribution of small craters reveals the effects of distal ejecta on lunar landscape morphology. *Icarus*, *326*, 63–87. https://doi.org/10.1016/j.icarus.2019.02.021
Moore, H. J., Hodges, C. A., & Scott, D. H. (1974). Multiringed basins—Illustrated by Orientale and associated features. In *The 5th Lunar and Planetary Science Conference*, pp. 71–100.
Morota, T., Haruyama, J., Honda, C., Ohtake, M., Yokota, Y., Kimura, J., et al. (2009). Mare volcanism in the lunar farside Moscoviense region: Implication for lateral variation in magma production of the Moon. *Geophysical Research Letters*, *36*, L21202. https://doi.org/10.1029/2009GL040472
Morota, T., Haruyama, J., Ohtake, M., Matsunaga, T., Honda, C., Yokota, Y., et al. (2011). Timing and characteristics of the latest mare eruption on the Moon. *Earth and Planetary Science Letters*, *302*(3), 255–266. https://doi.org/10.1016/j.epsl.2010.12.028
Nava, R. A. (2011). *Crater helper tools for ArcGIS 10.0 (U.S Geological Survey Reference Manual)*. Flagstaff: U.S. Geological Survey.
Nelson, D. M., Koeber, S. D., Daud, K., Robinson, M. S., Watters, T. R., Banks, M. E., & Williams, N. R. (2014). Mapping lunar maria extents and lobate scarps using LROC image products. In *The 45th Lunar and Planetary Science Conference*, pp. 2861.
Nesvorný, D., Morbidelli, A., Vokrouhlický, D., Bottke, W. F., & Brož, M. (2002). The Flora family: A case of the dynamically dispersed collisional swarm? *Icarus*, *157*(1), 155–172. https://doi.org/10.1006/icar.2002.6830
Neukum, G., & Horn, P. (1976). Effects of lava flows on lunar crater populations. *The Moon*, *15*(3–4), 205–222. https://doi.org/10.1007/BF00562238
Neukum, G., Ivanov, B., & Hartmann, W. (2001). Cratering records in the inner solar system in relation to the lunar reference system. *Space Science Review*, *96*(1-4), 55–86. https://doi.org/10.1023/A:1011989004263
Ohtake, M., Haruyama, J., Matsunaga, T., Yokota, Y., Morota, T., & Honda, C (2008). Performance and scientific objectives of the SELENE (Kaguya) Multiband Imager. *Earth, Planets and Space*, *60*(4), 257–264. https://doi.org/10.1186/BF03352789
Ono, T., Kumamoto, A., Nakagawa, H., Yamaguchi, Y., Oshigami, S., Yamaji, A., et al. (2009). Lunar Radar Sounder observations of subsurface layers under the nearside maria of the Moon. *Science*, *323*(5916), 909–912. https://doi.org/10.1126/science.1165988
Oshigami, S., Okuno, S., Yamaguchi, Y., Ohtake, M., Haruyama, J., Kobayashi, T., et al. (2012). The layered structure of lunar maria: Identification of the HF-radar reflector in Mare Serenitatis using multiband optical images. *Icarus*, *218*(1), 506–512. https://doi.org/10.1016/j.icarus.2011.12.026
Oshigami, S., Watanabe, S., Yamaguchi, Y., Yamaji, A., Kobayashi, T., Kumamoto, A., et al. (2014). Mare volcanism: Reinterpretation based on Kaguya Lunar Radar Sounder data. *Journal of Geophysical Research: Planets*, *119*, 1037–1045. https://doi.org/10.1002/2013JE004568
Oshigami, S., Yamaguchi, Y., Yamaji, A., Ono, T., Kumamoto, A., Kobayashi, T., & Nakagawa, H. (2009). Distribution of the subsurface reflectors of the western nearside maria observed from Kaguya with Lunar Radar Sounder. *Geophysical Research Letters*, *36*, L18202. https://doi.org/10.1029/2009GL039835
Ostrach, L. R., Robinson, M. S., Whitten, J. L., Fassett, C. I., Strom, R. G., Head, J. W., & Solomon, S. C. (2015). Extent, age, and resurfacing history of the northern smooth plains on Mercury from MESSENGER observations. *Icarus*, *250*, 602–622. https://doi.org/10.1016/j.icarus.2014.11.010
Otake, H., Ohtake, M., & Hirata, N. (2012). Lunar iron and titanium abundance algorithms based on SELENE (Kaguya) Multiband Imager data. In *The 43rd Lunar and Planetary Science Conference*, pp. 1905.
Pasckert, J. H., Hiesinger, H., & van der Bogert, C. H. (2018). Lunar farside volcanism in and around the South Pole-Aitken basin. *Icarus*, *299*, 538–562. https://doi.org/10.1016/j.icarus.2017.07.023
Peeples, W. J., Sill, W. R., May, T. W., Ward, S. H., Phillips, R. J., Jordan, R. L., et al. (1978). Orbital radar evidence for lunar subsurface layering in Maria Serenitatis and Crisium. *Journal of Geophysical Research*, *62*, 3459–3468. https://doi.org/10.1029/JB083iB07p0345

Phillips, R. J., Adams, G. F., Brown, W. E. Jr., Eggleton, R. E., Jackson, P., Jordan, R., et al. (1973). Apollo Lunar Sounder Experiment (*Apollo 17 Preliminary Science Report*) (pp. 22-1–22-26). Houston: NASA.

Pike, R. J. (1967). Schroeter's rule and the modification of lunar crater impact morphology. *Journal of Geophysical Research*, *72*(8), 2099–2106. https://doi.org/10.1029/JZ072i008p02099

Pike, R. J. (1972). Geometric similitude of lunar and terrestrial craters. In *The 24th International Geological Congress*, pp. 41–47.

Pike, R. J. (1974). Depth/diameter relations of fresh lunar craters: Revision from spacecraft data. *Geophysical Research Letters*, *1*(7), 291–294. https://doi.org/10.1029/GL001i007p00291

Pike, R. J. (1977). Size-dependence in the shape of fresh impact craters on the Moon, *Impact and explosion cratering: Planetary and terrestrial implications* (pp. 488–509). New York: Pergamon Press.

Pohn, H., & Offield, T. (1970). *Lunar crater morphology and relative-age determination of lunar geologic units–Part 1. Classification*. (pp. 153–162). Flagstaff: U. S. Geological Survey. https://doi.org/10.3133/ofr69209

Richardson, J. E. (2009). Cratering saturation and equilibrium: A new model looks at an old problem. *Icarus*, *204*(2), 697–715. https://doi.org/10.1016/j.icarus.2009.07.029

Robbins, S. J., Antonenko, I., Kirchoff, M. R., Chapman, C. R., Fassett, C. I., Herrick, R. R., et al. (2014). The variability of crater identification among expert and community crater analysts. *Icarus*, *234*, 109–131. https://doi.org/10.1016/j.icarus.2014.02.022

Robinson, M. S., Ashley, J. W., Boyd, A. K., Wagner, R. V., Speyerer, E. J., Hawke, B. R., et al. (2012). Confirmation of sublunarean voids and thin layering in mare deposits. *Planetary and Space Science*, *69*(1), 18–27. https://doi.org/10.1016/j.pss.2012.05.008

Robinson, M. S., Brylow, S. M., Tschimmel, M., Humm, D., Lawrence, S. J., Thomas, P. C., et al. (2010). Lunar Reconnaissance Orbiter Camera (LROC) instrument overview. *Space Science Review*, *150*(1-4), 81–124. https://doi.org/10.1007/s11214-010-9634-2

Schaber, G. G. (1973). Lava flows in Mare Imbrium: Geologic evaluation from Apollo orbital photography. In *The 4th Lunar and Planetary Science Conference*, pp. 653–655.

Schittkowski, K. (1986). NLPQL: A FORTRAN subroutine solving constrained nonlinear programming problems. *Annals of Operations Research*, *5*(2), 485–500. https://doi.org/10.1007/BF02022087

Sharpton, V. L., & Head, J. W. (1982). Stratigraphy and structural evolution of southern Mare Serenitatis: A reinterpretation based on Apollo Lunar Sounder Experiment data. *Journal of Geophysical Research*, *87*(B13), 10,983–10,998. https://doi.org/10.1029/JB087iB13p10983

Shoemaker, E. M. (1965). Preliminary analysis of the fine structure of the lunar surface in Mare Cognitum. In *The 5th International Astronomical Union Colloquium*, pp. 23–77. https://doi.org/10.1017/S0252921100115714

Smith, D. E., Zuber, M. T., Jackson, G. B., Cavanaugh, J. F., Neumann, G. A., Riris, H., et al. (2010). The Lunar Orbiter Laser Altimeter investigation on the Lunar Reconnaissance Orbiter mission. *Space Science Review*, *150*, 209–241. https://doi.org/10.1007/s11214-009-9512-y

Snape, J. F., Curran, N. M., Whitehouse, M. J., Nemchin, A. A., Joy, K. H., Hopkinson, T., et al. (2018). Ancient volcanism on the Moon: Insights from Pb isotopes in the MIL 13317 and Kalahari 009 lunar meteorites. *Earth and Planetary Science Letters*, *502*, 84–95. https://doi.org/10.1016/j.epsl.2018.08.035

Soderblom, L. A. (1970). A model for small-impact erosion applied to the lunar surface. *Journal of Geophysical Research*, *75*(14), 2655–2661. https://doi.org/10.1029/JB075i014p02655

Solomon, S. C., & Head, J. W. (1979). Vertical movement in mare basins: Relation to mare emplacement, basin tectonics, and lunar thermal history. *Journal of Geophysical Research*, *84*(B4), 1667–1682. https://doi.org/10.1029/JB084iB04p01667

Solomon, S. C., & Head, J. W. (1980). Lunar mascon basins: Lava filling, tectonics, and evolution of the lithosphere. *Reviews of Geophysics*, *18*(1), 107–141. https://doi.org/10.1029/RG018i001p00107

Sood, R., Chappaz, L., Melosh, H. J., Howell, K. C., Milbury, C., Blair, D. M., & Zuber, M. T. (2017). Detection and characterization of buried lunar craters with GRAIL data. *Icarus*, *289*, 157–172. https://doi.org/10.1016/j.icarus.2017.02.013

Speyerer, E., Robinson, M. S., & LROC Team (2011). Lunar Reconnaissance Orbiter Camera global morphological map of the Moon. In *The 42nd Lunar and Planetary Science Conference*, pp. 2387.

Stickle, A. M., Patterson, G. W., Cahill, J. T. S., & Bussey, D. B. J. (2016). Mini-RF and LROC observations of mare crater layering relationships. *Icarus*, *273*, 224–236. https://doi.org/10.1016/j.icarus.2016.03.014

Stöffler, D., & Ryder, G. (2001). Stratigraphy and isotope ages of lunar geologic units: Chronological standard for the inner solar system. *Space Science Review*, *96*(1-4), 9–54. https://doi.org/10.1023/A:1011937020193

Talwani, M., Thompson, G., Dent, B., Kahle, H.-G., & Buck, S. (1973). Traverse gravimeter experiment (*Apollo 17 Preliminary Science Report*). (pp. 13-1–13-13). Houston: NASA.

Thomson, B. J., Grosfils, E. B., Bussey, D. B. J., & Spudis, P. D. (2009). A new technique for estimating the thickness of mare basalts in Imbrium Basin. *Geophysical Research Letters*, *36*, L12201. https://doi.org/10.1029/2009GL037600

Weider, S. Z., Crawford, I. A., & Joy, K. H. (2010). Individual lava flow thicknesses in Oceanus Procellarum and Mare Serenitatis determined from Clementine multispectral data. *Icarus*, *209*(2), 323–336. https://doi.org/10.1029/2009GL037600

Werner, S. C., & Medvedev, S. (2010). The Lunar rayed-crater population—Characteristics of the spatial distribution and ray retention. *Earth and Planetary Science Letters*, *295*(1–2), 147–158. https://doi.org/10.1016/j.epsl.2010.03.036

Wessel, P., & Smith, W. H. F. (1991). Free software helps map and display data. *EOS Transactions American Geophysical Union*, *72*(41), 441–446. https://doi.org/10.1029/90EO00319

Wilson, L., & Head, J. W. (1981). Ascent and eruption of basaltic magma on the Earth and Moon. *Journal of Geophysical Research*, *86*(B4), 2971–3001. https://doi.org/10.1029/JB086iB04p02971

Wilson, L., & Head, J. W. (2017). Generation, ascent and eruption of magma on the Moon: New insights into source depths, magma supply, intrusions and effusive/explosive eruptions (Part 1: Theory). *Icarus*, *283*, 146–175. https://doi.org/10.1016/j.icarus.2016.05.031

Xiao, L., Zhu, P., Fang, G., Xiao, Z., Zou, Y., Zhao, J., et al. (2015). A young multilayered terrane of the northern Mare Imbrium revealed by Chang'E-3 mission. *Science*, *347*(6227), 1226–1229. https://doi.org/10.1126/science.1259866

Xie, M., & Zhu, M. H. (2016). Estimates of primary ejecta and local material for the Orientale basin: Implications for the formation and ballistic sedimentation of multi-ring basins. *Earth and Planetary Science Letters*, *440*, 71–80. https://doi.org/10.1016/j.epsl.2016.02.012

Xie, M., Zhu, M.-H., Xiao, Z., Wu, Y., & Xu, A. (2017). Effect of topography degradation on crater size-frequency distributions: Implications for populations of small craters and age dating. *Geophysical Research Letters*, *44*, 10,171–10,179. https://doi.org/10.1002/2017GL075298

Zhang, J., Yang, W., Hu, S., Lin, Y., Fang, G., Li, C., et al. (2015). Volcanic history of the Imbrium basin: A close-up view from the lunar rover Yutu. *Proceedings of the National Academy of Sciences*, *112*, 5342–5347. https://doi.org/10.1073/pnas.1503082112

Zhang, F., Zhu, M.-H., Bugiolacchi, R., Huang, Q., Osinski, G. R., Xiao, L., & Zou, Y. L. (2018). Diversity of basaltic lunar volcanism associated with buried impact structures: Implications for intrusive and extrusive events. *Icarus*, *307*, 216–234. https://doi.org/10.1016/j.icarus.2017.10.039